1 **Title**

2 RIVER FLOOD MAPPING IN URBAN AREAS COMBINING RADARSAT-2 DATA AND FLOOD

3 RETURN PERIOD DATA

4

5 **Author names and affiliations**

6 Marion Tanguy [a*], Karem Chokmani [a], Monique Bernier [a], Jimmy Poulin [a], Sébastien Raymond [a]

7 [a] Institut National de la Recherche Scientifique, Centre Eau Terre Environnement, 490 rue de la

8 Couronne, G1K 9A9 Québec (QC) Canada.

9 *E-mail:* karem.chokmani@ete.inrs.ca (K.C); monique.bernier@ete.inrs.ca (M.B);

10 jimmy.poulin@ete.inrs.ca (J.P); sebastien.raymond@ete.inrs.ca (S.R)

11

12 *** Corresponding author:** Tel: +1 1418 654 2530 – 4466

13 E-mail: marion.tanguy@ete.inrs.ca (M. Tanguy)

14

15

16

17

18

19

20

21

22

Abstract

Near-real-time flood maps are essential to organize and coordinate emergency services' response actions during flooding events. Thanks to its capacity to acquire synoptic and detailed data during day and night, and in all weather conditions, Synthetic Aperture Radar (SAR) satellite remote sensing is considered one of the best tools for the acquisition of flood mapping information. However, specific factors contributing to SAR backscatter in urban environments, such as shadow and layover effects, and the presence of water surface–like radar response areas, complicate the detection of flood water pixels. This paper describes an approach for near-real-time flood mapping in urban and rural areas. The innovative aspect of the approach is its reliance on the combined use of very-high-resolution SAR satellite imagery (C-Band, HH polarization) and hydraulic data, specifically flood return period data estimated for each point of the floodplain. This approach was tested and evaluated using two case studies of the 2011 Richelieu River flood (Canada) observed by the very-high-resolution RADARSAT-2 sensor. In both case studies, the algorithm proved capable of detecting flooding in urban areas with good accuracy, identifying approximately 87% of flooded pixels correctly. The associated false negative and false positive rates are approximately 14%. In rural areas, 97% of flooded pixels were correctly identified, with false negative rates close to 3% and false positive rates between 3% and 35%. These results highlight the capacity of flood return period data to overcome limitations associated with SAR-based flood detection in urban environments, and the relevance of their use in combination with SAR C-band imagery for precise flood extent mapping in urban and rural environments in a crisis management context.

1. Introduction

The capacity of spaceborne Synthetic Aperture Radar (SAR) remote sensing for near-real-time flood detection and mapping has been demonstrated by numerous studies over the last decade (Henry et al., 2006, Greifeneder et al., 2014, Schumann et al., 2011; Schumann et al., 2012; Pulvirenti et al., 2014). Many civil protection organizations now use airborne and satellite SAR imagery to support the development of assistance plans to reduce human and material consequences of flooding events (Bhatt et al., 2016 ; Boni et al., 2009 ; Kussul et al., 2014 ; Martinis et al., 2015 ; Pulvirenti et al., 2013 ; Zhang et al., 2002).

Accurate flood detection is of the utmost importance in urban areas, where high population concentrations and critical infrastructures often make the economic and social impacts of a flood event very high. However, specific factors contributing to SAR backscatter hamper flood water detection in built-up environments. In particular, the side-looking nature of SAR sensors can cause objects such as buildings and tall vegetation, oriented parallel or roughly parallel to the satellite track, to produce shadow and layover effects (Soergel et al., 2010). The magnitude of these geometric distortions, which may hide important sections of the ground from the sensor, is a function of wavelengths, radar look angle, and polarization (Mason et al., 2014; Schumann et al., 2009). In addition, large, permanent, specular-like reflection surfaces typical of urban areas, such as roads and parking lots, may be confused with open water regions, thereby increasing flood detection errors (Mason et al., 2010).

In order to limit the impact of these effects on flood detection accuracy, the methods that have been developed for flood detection in urban areas using SAR imagery have taken advantage of a variety of tools and sources of ancillary information. For instance, in the algorithm for near-real-time flood detection in urban areas using TerraSAR-X images presented by Mason et al. (2010; 2012), a SAR end-to-end simulator (Speck et al., 2007) was run in conjunction with high-

73 resolution LIDAR data of the urban area of Tewkesbury (UK) to generate a map of shadow and

74 layover effects. Masking these effects during near-real-time processing enabled 75% of the

75 unmasked flooded pixels to be correctly classified in urban areas. Furthermore, in Mason et al.

76 (2014), the same SAR simulator and high-resolution LIDAR data were successfully used in a

77 double-scattering strength measurement method for flood detection in the layover regions of the

78 same TerraSAR-X image.

79 In Giustarini et al. (2013), areas affected by shadow effects, permanent water surfaces, and

80 other surfaces characterized by specular-like reflections are identified by detecting changes in

81 backscatter intensities between a high-resolution TerraSAR-X flood image and a non-flooded

82 reference image. These areas are then masked out from the final flood map to reduce false

83 alarms.

84 In addition, Chini et al. (2012) and Pulvirenti et al. (2015) demonstrated that combining the

85 complex coherence information extracted from COSMO-SkyMed interferometric pairs with

86 intensity information can greatly assist in the detection of flooded areas in both urban and rural

87 environments and reduce flood detection omissions produced by approaches based solely on

88 intensity analysis.

89 These algorithms enable flood water detection in urban areas with reasonable accuracy, but it is

90 worth mentioning that the use of shadow and layover masks results in non-identification of the

91 flooding status of a significant part of the flooded urban areas (e.g., 39% in the study by

92 Giustarini et al. (2013)). Moreover, the availability of an adequate non-flooded SAR reference

93 image (identical orbit track and polarization, similar state of vegetation, etc.), required by a

94 change-detection approach, of a SAR simulator, or of adequate SAR interferometric pairs, is not

95 always guaranteed.

96   Simple hydraulic considerations have also been used in several image-processing algorithms to

97   guide the detection of flooded pixels in urban and rural areas (see Pierdicca et al., 2008 ;

98   Pulvirenti et al., 2011 ; Mason et al., 2012 or Schumann et al., 2011). In this approach,

99   information from surface elevation data, which have the advantage of being available for most

100 rivers worldwide, is exploited. However, such algorithms restrict the integration of hydraulic

101 considerations to simple elevation and proximity analysis. To our knowledge, no example can

102 be found in the recent literature of the explicit integration of hydraulic data within SAR image-

103 processing algorithms for flood detection in urban and rural areas. Such data, which could

104 include information about a river's flooding pattern or the specific hydraulic characteristics of a

105 floodplain, could be of great use in areas where SAR-based flood detection remains a

106 challenge.

107 Therefore, the objective of the present study is to demonstrate how a combination of very high

108 resolution SAR imagery and hydraulic data can yield effective near-real time flood delineation in

109 urban areas. More specifically, we rely on the use of the flood return period, estimated at each

110 point of the floodplain. Note that the flood return period, which can be defined here as the

111 average number of years between two flood occurrences of the same magnitude, will be

112 referred to as "RP" in the following sections. The underlying hypothesis is that this parameter,

113 which relates to the hydrologic and hydraulic characteristics of the floodplain and the flooding

114 event, might allow the identification of flooded pixels, even in areas where SAR remote sensing

115 is limited. In order to confirm this hypothesis, an innovative approach was developed and

116 evaluated by using two very-high-resolution RADARSAT-2 images (C-Band, HH polarization)

117 acquired during the 2011 Richelieu River flood (Canada) with different acquisition parameters

118 and water surface conditions.

119

2. Methodology

The proposed method (depicted in the flowchart in Fig. 1) provides near-real-time flood extent mapping in urban and rural areas using a high-resolution SAR C-Band HH-polarized flood image as input data. Horizontal polarization is preferred over vertical polarization or cross polarization as it generally yields the highest contrast between open water and upland locations (Brisco et al., 2008). The SAR image must be speckle-filtered (Senthilnath et al., 2013), geocoded, and calibrated to obtain backscatter values.

RP data estimated for each point of the study area are also required. These values are generally estimated using one dimensional (1D) or two-dimensional (2D) hydraulic modelling. If such data is not available for the study area, an alternative method for RP estimation at each point of the study area is described in section 2.1. This estimation should be carried out prior to near-real-time operations.

Fig. 1: Flowchart of the proposed approach.

The first step in near-real-time operations is the detection of open water flooded areas on SAR

flood image using an approach that combines object-oriented segmentation, calibration of the

138   statistical distribution of "open water" objects' mean backscatter values, and thresholding-based

139   fuzzy classification. This initial classification of "open water" objects is then refined using the

140   degree of membership of each object in the "open water" set and its maximum RP. Following

141   this classification refinement, the RP associated with the maximum extent of the refined "open

142   water" classification is extracted. Finally, floodplain points for which the RP is less than or equal

143   to this maximum RP are selected to create the final flood map. These near-real-time processing

144   steps will be described in detail in the following sections.

145

146   *2.1 Method for flood return period estimation*

147

148   RPs are usually computed, for some selected RPs, using a 1D or 2D hydraulic model forced by

149   statistically estimated hydrological inputs. Hydrological and hydraulic models, set up for a given

150   area, are generally not available for the public. However, their outputs in terms of RP shorelines

151   or extents are publicly released, for some selected RPs. Between 3 and 5 RP shorelines are

152   usually made available, depending on the country or region, and are widely used as risk criteria

153   for land use planning. Therefore, the RP of most points of the floodplain remain unknown.

154   Running a hydraulic simulation can be complex and time consuming. We hereby propose a

155   simple and efficient method to estimate the RP at each point of the floodplain, based on the

156   available RP shorelines in the study area and on topographic elevation data. A flowchart of this

157   method is presented in Fig. 2.

158
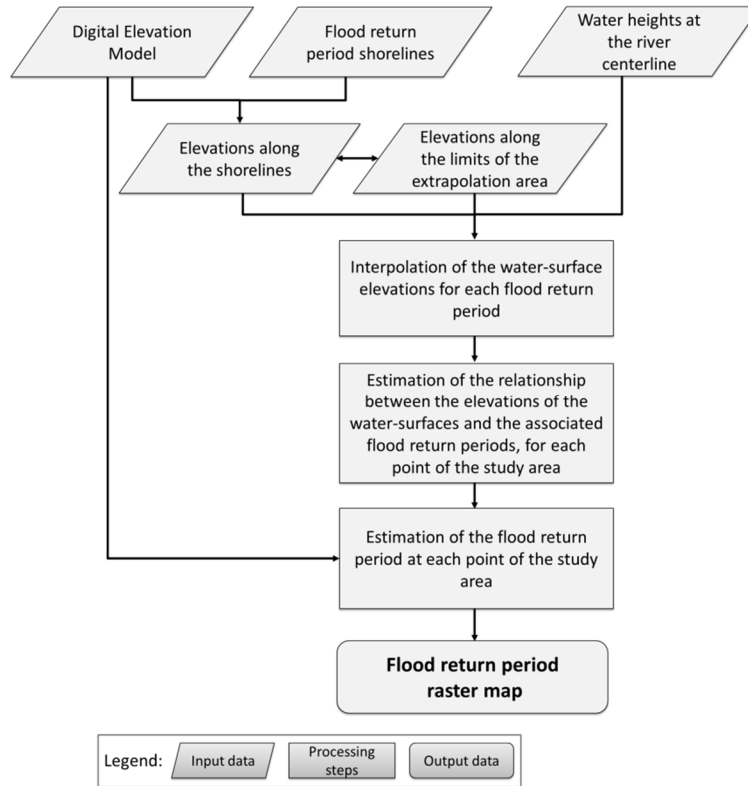
Fig. 2: Flowchart of the flood return period raster map estimation.

159

160

161   The inputs to this method are:

162   1. Available RP shorelines for the river. The positions of such shorelines along the river are

163   estimated using 1D or 2D hydraulic modelling, and they are often made available in the

164   form of polygons or polylines. A minimum of three different RP floodplain shorelines are

165   required to estimate consistent RP at each point of the floodplain.

166   2. Water height values at the river centreline associated with each RP shoreline available.

167   The water-surface elevations at the river centreline are also estimated by using either a

168   1D hydraulic model (in which case one value of water height at the river centreline

169   coincides with the values of water height of the given section) or a 2D hydraulic model

170   (in which case a water height value is available for each cell of the model at the river

171   centreline, including one value for each cell located along the river centreline).

172   3. A high-resolution digital elevation model (DEM) of the ground elevations in the area. In

173   order to allow extraction of accurate water levels along the RP shorelines, this DEM

174   should be the same as the one used to estimate the position of these shorelines. If this

175   DEM is not available, a DEM with identical vertical and horizontal accuracies must be

176   used. Also, the user must ensure that no major changes in ground elevations occurred

177   between the time the flood return shorelines were estimated and the time the alternative

178   DEM was produced. It should be noted that the higher the vertical and horizontal

179   accuracies of the DEM used are, the more precise the RP estimation at each point of the

180   floodplain should be.

181

182 RP estimation at each point of the floodplain follows three steps. In order to facilitate

183 understanding of this procedure, its different elements are gathered in a single figure (see Fig.

184 3), which also presents an example of RP of a point in the floodplain.

Example of RP estimation at a point in the floodplain
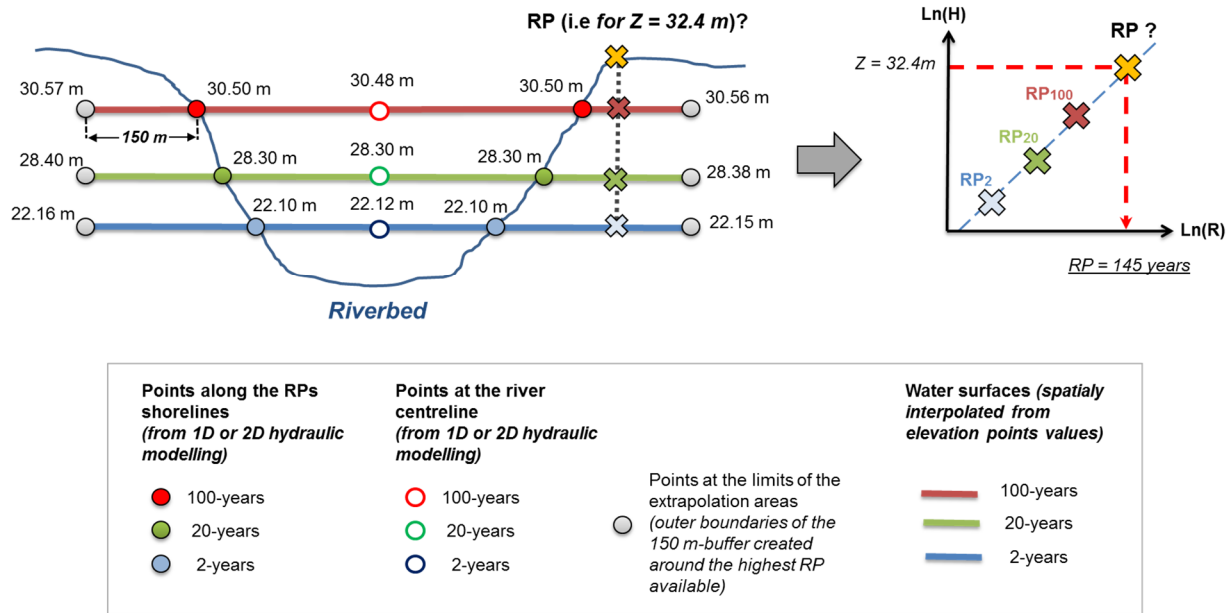
Fig. 3: General scheme of RP estimation at a given point in the floodplain.

First, the elevations of the water surface associated with each RP are generated, using a spatial interpolation technique. This involves the creation and aggregation of the points used for the generation of each water surface. To do so, each RP shoreline is converted into feature points and the elevations of these points are extracted from the DEM. For each RP available, a set of points is created by grouping the water height feature points at the river centreline with the feature points along the RP shoreline. Then, a 150 m-buffer is created around the shorelines of the highest RP available, and its outer boundaries are converted into feature points. These points represent the extrapolation area limits, which allow to estimate the RP for the points of the study area located outside the highest RP available. These points are added to each RP set of points. By doing so, we ensure that all the RPs water surfaces will have the same number of rows and columns. The elevation of each point located along the extrapolation area is estimated using the k-nearest neighbour regression method (Altman, 1992), based on the elevation of the 100 nearest points located along the RP shoreline. Finally, each RP water surface is spatially

11

201 interpolated from its set of points, which is now composed of the river centreline points, along

202 the RP shoreline and the outer limits of the extrapolation area. The interpolation is done using a

203 natural neighbour interpolation technique (Sibson, 1981). The RPs water surfaces created are

204 raster surfaces with the same number of rows and columns, in which cell values represent the

205 water surface elevation, for a given RP. Their spatial resolution is set to be the same as the

206 spatial resolution of the DEM used.

207 Second, for each cell common to all the RP raster water surfaces previously created, the

208 relationship between water height at the cell location and the RPs associated with these water

209 heights is estimated. For instance, if 3 RPs water surfaces with the same number of rows and

210 columns have been generated, this relationship will be estimated for each cell using 3 water

211 heights and 3 RPs. This relationship is expressed by the following non-linear regression

212 function:

$$H = \alpha R^{\beta} \qquad (1)$$

213

214 where H is the water surface elevation at the cell position (in metres), extracted from the water

215 surface raster, and R is the RP associated with that water surface (in years). α and β are the

216 non-linear regression parameters to be estimated.

217 Lastly, RP is estimated for each point of the floodplain using the elevation of the cell and the α

218 and β parameters specific to that cell. RPs are estimated using the following equation:

$$R = \left(\frac{Z}{\alpha}\right)^{\frac{1}{\beta}} \qquad (2)$$

219

220 where Z is the elevation of the cell, extracted from the high-resolution DEM of the area, and α

12

221   and β are the parameters of the non-linear regression previously estimated for the cell. R is the

222   RP of the cell, in years, and represents the return period at which the area represented by the

223   cell should be flooded.

224   The results are stored in a raster map, which will be designated as the "flood return period map"

225   in the following steps of the method. The spatial resolution of this raster map must be the same

226   as the spatial resolution of the DEM used. The estimated RPs are expressed per cell, in years.

227   It is worth mentioning that even if the use of an extrapolation technique is essential to estimate

228   the RP of the points located above the shoreline of the highest RP available, as well as between

229   the shorelines of the lowest and highest RP available, it also leads to less reliable RP

230   estimations. This can be considered as a limitation of this method. However, and this is an

231   important point, the RPs estimated at each point of the floodplain using this method are relative

232   values, which are not considered as representative of the water discharge needed to flood this

233   point. These values should rather be regarded as indicators of the potential RP of a cell,

234   considering its position and elevation in the floodplain with respect to the characteristics of the

235   RP shorelines available.

236

237   *2.2 Segmentation of the SAR image*

238

239   High-resolution SAR data enables precise detection of individual features on the earth's surface,

240   but the use of high spatial resolution also results in significant within class backscatter variances

241   and therefore, high inter-class spectral confusion (Voigt et al., 2008; Martinis et al., 2011). This

242   makes high-resolution SAR image processing with traditional per-pixel methods challenging,

243   and the generated results may be affected by inherent speckle noise of SAR imagery (Esch et

244 al., 2006). If the application of speckle filters helps to reduce this effect, speckle noise remains

245 at least partially present (Senthilnath et al., 2013). An alternative to per-pixel methods is object-

246 based classification. Objects are created by the sequential merging of neighbouring pixels

247 based on similarity criteria, such as their spectral characteristics, their shape, or their texture.

248 This results in non-overlapping homogeneous objects that correlate with real-world objects

249 (Blaschke et al., 2014). One of the advantages of the object-based approach is that it provides a

250 preliminary delineation of open water areas, through objects readily usable for classification

251 (Blaschke et al., 2010).

252 Segmentation of high-resolution SAR flood images into objects is performed by using the multi-

253 resolution segmentation module of the eCognition Developer 8 software. This algorithm has

254 already proved successful at segmenting rural open water areas in a high-resolution TerraSAR-

255 X image, in a study by Mason et al. (2012). This image segmentation algorithm is a bottom-up

256 segmentation method based on a pairwise region-merging technique (Definiens AG, 2011).

257 Segmentation begins with single-pixel objects, which are iteratively merged with neighbouring

258 pixels until the object's growth exceeds the maximum allowed heterogeneity criterion set by the

259 user through a scale parameter. The object homogeneity criterion is defined by a combination of

260 spectral values (or colour) and shape properties, based on smoothness and compactness

261 criteria. As open water areas are generally characterized by dark tones and irregular shapes,

262 the shape criterion is set low to increase the relative contribution of spectral values in the

263 homogeneity criterion, and the compactness value is set medium to limit over-segmentation of

264 open water objects due to local variations in backscatter values. After trial-and-error

265 experimentation with the segmentation procedure, a shape value of 10% and a compactness

266 value of 50% were selected. The scale parameter was set to 5, to enable estimation of the

267 statistical distribution of "open water" on a large amount of data representatives of the class.

268

269   *2.3 Statistical estimation of "open water" object backscatter*

270

271   Next, the probability density function (PDF) of the mean backscatter values of the SAR image

272   objects associated with open water must be estimated. This method was successfully applied in

273   Matgen et al. (2011) and in Giustarini et al. (2013) for open water area detection on ENVISAT

274   and TerraSAR-X flood images, respectively. In these two studies, the statistical distribution of

275   "open water" backscatter values was estimated using a gamma PDF to extract the parameters

276   of a region-growing approach. The choice of a gamma PDF was based on previous work by

277   Ulaby et al. (1986), who ascertained that the PDF of homogeneous surfaces with backscatter

278   variability, which is mainly due to speckle, is of the gamma type. Alternative PDF types, such as

279   the K-distribution and the RiIG distribution functions, were tested by Giustarini et al. (2013) and

280   found not to provide more precise empirical distribution-fitting than a gamma function.

281   The gamma probability density function used for estimating the mean statistical distribution of

282   open water object backscatter can be expressed as follows:

$$f(\sigma^0|k,\theta) = \frac{(\sigma^0 - \sigma_1^0)^{k-1}}{\theta^k \Gamma(k)} \cdot e^{-\frac{(\sigma^0 - \sigma_1^0)}{\theta}} \tag{3}$$

283

284   Where σ^0 represents the backscatter value of each pixel in the SAR image, expressed in dB; k

285   is the shape parameter of the gamma distribution, and θ is the scale parameter. As gamma

286   distribution is computable only for positive values, the backscatter values are shifted to positive

287   for the entire range of empirical values. Therefore, the parameter σ_1^0 represents the minimum

288   backscatter value of the SAR image, in dB.

289

290   The following formula of the gamma distribution mode was used to facilitate the fitting procedure

291   (Matgen et al., 2011): When $k \geq 1$,

$$\sigma_m^0 = (k-1).\theta + \sigma_1^0. \tag{4}$$

292

293   The gamma probability density function can thus be expressed as:

$$f_{\sigma_m^0}(\sigma^0|k) = \frac{\left(\sigma^0 - \sigma_1^0\right)^{k-1}}{\left(\frac{\left(\sigma_m^0 - \sigma_1^0\right)}{k-1}\right)^k . \Gamma(k)} e^{-\frac{\left(\sigma^0 - \sigma_1^0\right).(k-1)}{\left(\sigma_m^0 - \sigma_1^0\right)}}. \tag{5}$$

294

295   Therefore, for a given value of σ_m^0 (in dB), only the k value has to be optimized to determine

296    $f_{\sigma_m^0}$. A local maxima estimator, which searches for the mode value with the highest probability

297   density in the lowest backscatter values, is used to automatically set a first-guess value for the

298   σ_m^0 parameter. Then, for all plausible values close to σ_m^0, the k parameter is iteratively optimized

299   using a non-linear least square fitting process. Note that the search interval at each iteration is

300   automatically set by the non-linear least square regression fitting process, based on the Port

301   algorithm for non-linear least squares (Fox et al., 1977). For each set of σ_m^0 and k parameter

302   values, the Root Mean Square Error (RMSE) between the theoretical density function f and the

303   empirical density function is estimated. The values of the σ_m^0 and k parameters providing the

304   lowest RMSE are set as the optimum parameters for the estimation of the gamma PDF of the

305   open water object mean backscatter values.

306   If part of the open water area on the SAR flood image is affected by wind or rainfall, the

307   histogram of image objects mean backscatter values might not be bimodal. In such cases, the

308   algorithm is automatically directed towards an alternative option. The algorithm estimates the

309   first derivative of the cubic smoothing spline fitted on the experimental PDF of the mean

16

310 backscattering values of the SAR image objects. The first local positive minimum of the first

311 derivative, which represents the first point where the spline stops increasing or reaches a

312 plateau, is set as a first-guess value for the σ_m^0 parameter. The optimal σ_m^0 and k parameters

313 are then estimated using the previously described method. However, the proposed approach is

314 not applicable if the image object's histogram of mean backscatter values is strictly unimodal.

315 This may happen if the SAR image is dominated by water or land surfaces, if most open water

316 surfaces of the SAR image are affected by wind, or if the open water areas are small. This is a

317 limitation of this approach.

318

319 *2.4 Fuzzy rule–based classification of "open water" objects*

320

321 The fourth step is the classification of "open water" objects in the SAR flood image (Fig. 1). To

322 account for potential overlap of the backscatter values of open water surfaces and those of

323 other land use types, a fuzzy rule–based classification method is used (Macina et al., 2006).

324 Like traditional classification using a single threshold, fuzzy set theory eventually results in a

325 binary classification. However, one of the advantages of fuzzy set theory is that it also enables

326 estimation of the degree of membership of the elements of a fuzzy set (in this case, SAR image

327 objects) in a given class. A standard Z-shaped fuzzy membership function is used to assess the

328 SAR image object's membership to the "open water" class (Pulvirenti et al., 2013). According to

329 this function, the lower the image object's backscatter value, the higher its membership degree

330 to the class. The standard Z-shaped fuzzy membership function is expressed by:

$$f(\sigma_x^0, \sigma_1^0, \sigma_2^0) = \begin{cases} 1, & \sigma_x^0 \leq \sigma_1^0 \\ 1 - 2\left(\dfrac{\sigma_x^0 - \sigma_1^0}{\sigma_2^0 - \sigma_1^0}\right)^2, & \sigma_1^0 \leq \sigma_x^0 \leq \dfrac{\sigma_1^0 + \sigma_2^0}{2} \\ 2\left(\dfrac{\sigma_x^0 - \sigma_2^0}{\sigma_2^0 - \sigma_1^0}\right)^2, & \dfrac{\sigma_1^0 + \sigma_2^0}{2} \leq \sigma_x^0 \leq \sigma_2^0 \\ 0, & \sigma_x^0 \geq \sigma_2^0 \end{cases} \tag{6}$$

331

332 where σ_x^0 is the mean backscatter value (in dB) of the object for which the membership degree

333 is estimated and σ_1^0 and σ_2^0 are the fuzzy threshold parameters of the membership function, and

334 are expressed in dB.

335 The parameters σ_1^0 and σ_2^0 of the fuzzy set are automatically extracted from the theoretical

336 values of the gamma probability density function fitted on the open water object mean

337 backscatter values. Parameter σ_1^0 is set as the mode parameter of the theoretical "open water"

338 gamma distribution. This is considered the maximum backscatter value at which no overlap

339 between open water and other land use type backscatter values should happen. Parameter σ_2^0

340 is set as the 99th percentile of the theoretical "open water" gamma distribution (Matgen et al.,

341 2011). This high percentile value may induce some over-detection, as the tail of the "open

342 water" gamma distribution may largely overlap with the backscatter values of the other land use

343 types. However, it should also enable the inclusion of open water objects whose mean

344 backscatter values are affected by protruding vegetation or small-scale anthropogenic elements.

345 This first level classification is defined as the initial classification of "open water" objects.

346

347

348

2.5 Refinement of "open water" object classification

Next, the classification of "open water" objects is refined in order to reduce over-detection of

open water areas (see Fig.1). This refinement will have no impact on the under-detections

resulting from the application of the fuzzy rule-based classification, as objects whose mean

backscatter is higher than the value of parameter σ_2^0 are definitively excluded from "open water"

classification.

Two characteristics of the objects classified as "open water" are used for classification

refinement: their membership degree to the "open water" class and their RP value, extracted

from the flood return period map. Before proceeding with the refinements steps, objects located

outside the area covered by the RP map (that is, beyond the limits of the extrapolation area),

are automatically excluded from "open water" classification, as their location is considered too

far from the main river channel to be flooded.

The first classification refinement step uses the object's membership degree to the "open water"

class. Objects whose membership degree is superior or equal to 0.5 are selected. Then, objects

whose membership degree is inferior to 0.5, but whose border has a connection of at least one

pixel with the border of an object whose degree of membership is superior or equal to 0.5, are

also included in the selection. Despite the low membership degree of these objects to the "open

water" class, the spatial connection between these objects and objects with a high degree of

membership in the class indicates a high probability of being actually flooded. It is worth

mentioning that hedgerows or wind-affected water surfaces should not be included in adjacent

flooded objects by this rule. Indeed, the diffuse surface scattering of wind-affected surfaces and

the diffuse volume scattering of hedgerows result in objects with high mean backscattering

values. These values should be notably higher than the value of parameter σ_2^0, which

373   determines the higher threshold of the Z-shaped fuzzy membership function used for open

374   water fuzzy logic classification. Therefore, these objects have a membership value of "0" to the

375   "open water" class and are permanently rejected from the classification.

376   The second classification refinement step uses the RP of "open water" objects. Then, the

377   maximum RP of each object selected in the previous classification refinement step is calculated

378   using the flood return period map. To limit non-water pixels from being erroneously included in

379   the objects during the multi-resolution segmentation, the 99th percentile of the RP of the object

380   is considered as the maximum RP.

381   Objects corresponding to permanent water surfaces, such as the main river channel, lakes, and

382   reservoirs may be numerous, and the very low RP of these objects is likely to influence the

383   results of the final classification refinement step. Therefore, objects for which the RP's 99th

384   percentile is less than one year are removed from the selection.

385   Next, all the selected "open water" objects are merged together to create one single "open

386   water" object. The maximum RP of this object is extracted from the flood return period map. To

387   limit the influence of misclassified pixels on the RP estimate, the 99th percentile of the

388   maximum RP is used.

389   Finally, the objects classified as "open water" in the initial fuzzy logic classification but whose

390   RP's 99th percentile is inferior or equal to the previously computed maximum RP are included in

391   the final "open water" refined classification.

392

393

394

395　*2.6 Creation of the flood map in urban and rural areas*

396

397　Flood map creation for both the urban and the rural areas relies on two reasonable

398　assumptions. The first is that classification of the "open water" areas enables detection of the

399　maximum extent of the flood. The second is that an object whose RP is less than or equal to

400　that of the maximum extent of the flood can logically be considered flooded.

401　The method used for the final flood extent mapping in urban and rural areas follows two steps.

402　First, the maximum RP of the refined "open water" classification is estimated using the flood

403　return period map. To limit the impact of non-water pixels erroneously included in the "open

404　water" objects, the 99th percentile of the RP is used again. Every cell of the flood return period

405　raster map whose RP is inferior or equal to this maximum RP are then selected. The selected

406　cells represent the maximum extent of the flood in urban and rural areas at the time of SAR

407　image acquisition.

408

409　**3. Case study**

410

411　*3.1 Flooding event*

412

413　The data used to test the proposed method were acquired during the 2011 Richelieu River

414　flood, in southern Quebec, Canada. This river flows from south to north in the Saint Lawrence

415　lowlands, an area characterized by low relief and gentle slopes. From mid-April to the end of

416　June 2011, the Richelieu River was subject to major flooding that resulted from the melt of large

417　quantities of snow accumulated during the winter and unusually heavy and continued rainfalls

418 between mid-April and May. The river exceeded its bankfull discharge (1064 m³/s; 27.07 m in

419 gauged level, relative to sea level, at the Rapid Fryers gauging station) on April 17th, when the

420 flow increased to 1080 m³/s (27.58 m in gauged level). Water levels continued to rise and

421 reached their peak on May 6th, with a discharge of 1550 m³/s (30.21 m in gauged level). The

422 water level began to decrease only on June 2nd, and it took three more weeks, until June 22nd,

423 for the Richelieu River to return to below bankfull. This major event resulted in the flooding of

424 numerous urban and residential areas located along the river and of large areas of rural land.

425 More than 2500 buildings were flooded, and around 1600 people were forced to evacuate their

426 homes (OSCQ, 2013).

427 The majority of the buildings in this area are one or two stories high, with basements. Some

428 industrial warehouses and shopping centers, featuring large parking lots, are located in the area

429 of interest. Streets are organized in a grid pattern, which makes this area rather representative

430 of typical medium-sized towns in Canada.

431

432 *3.2 RADARSAT-2 images*

433

434 Two RADARSAT-2 (C-Band) images are available to assess the performance of the proposed

435 method. Their characteristics are summarized in Table 1. The first image is an Ultra-Fine Mode

436 Scene acquired on May 1, 2011 at 07:14 am local time, in HH polarization, during a descending

437 orbit pass (Fig. 4A). This image is a SAR Georeferenced Fine (SGF) product, with 1.5 x 1.5 m

438 pixel spacing (3 x 3 m after pixel resampling) and a mean incidence angle of 23°. No rainfall

439 was recorded in the 72 hours preceding the time of image acquisition, resulting in unsaturated

440 soil conditions in the non-flooded areas. Wind speed was moderate (7 km/h, blowing from east),

441 but the steep incidence angle (23°) of this SAR image makes it sensitive to Bragg resonance

442   effects. Bragg resonance leads to increased backscatter from open water surfaces, which can

443   be seen in Fig. 4C.

444   Table 1: Characteristics of the RADARSAT-2 flood images used to test the proposed method

Acquisition date and time (local time)	Acquisition type	Polarization	Track	Pixel Spacing (m)	Ground Resolution (m)	Product type	Average mean incidence angle (°)	Wind speed at the time of acquisition
May 1, 2011 06:14 am	Ultra-Fine	HH	Descending	1.56x1.56	3	SGF	22.5	7 km/h
May 7, 2011 06:59 pm	Fine	HH-HV	Ascending	4.7x5.1	8	SLC	48	11 km/h

445

446   The second SAR image is a Fine Mode Scene acquired on May 7 at 06:59 pm local time, in HH-

447   HV polarization, during an ascending orbit pass (Fig. 4B). Only the HH polarization was used.

448   This image is a Single Look Complex (SLC) product, with 4.7 x 5.1 m pixel spacing (8 x 8 m

449   after pixel resampling) and a mean incidence angle of 48°. Significant rainfalls (> 70 mm) were

450   recorded in the four days before image acquisition, resulting in wet soil conditions in the non-

451   flooded areas. Winds were blowing at 11 km/h from northeast.
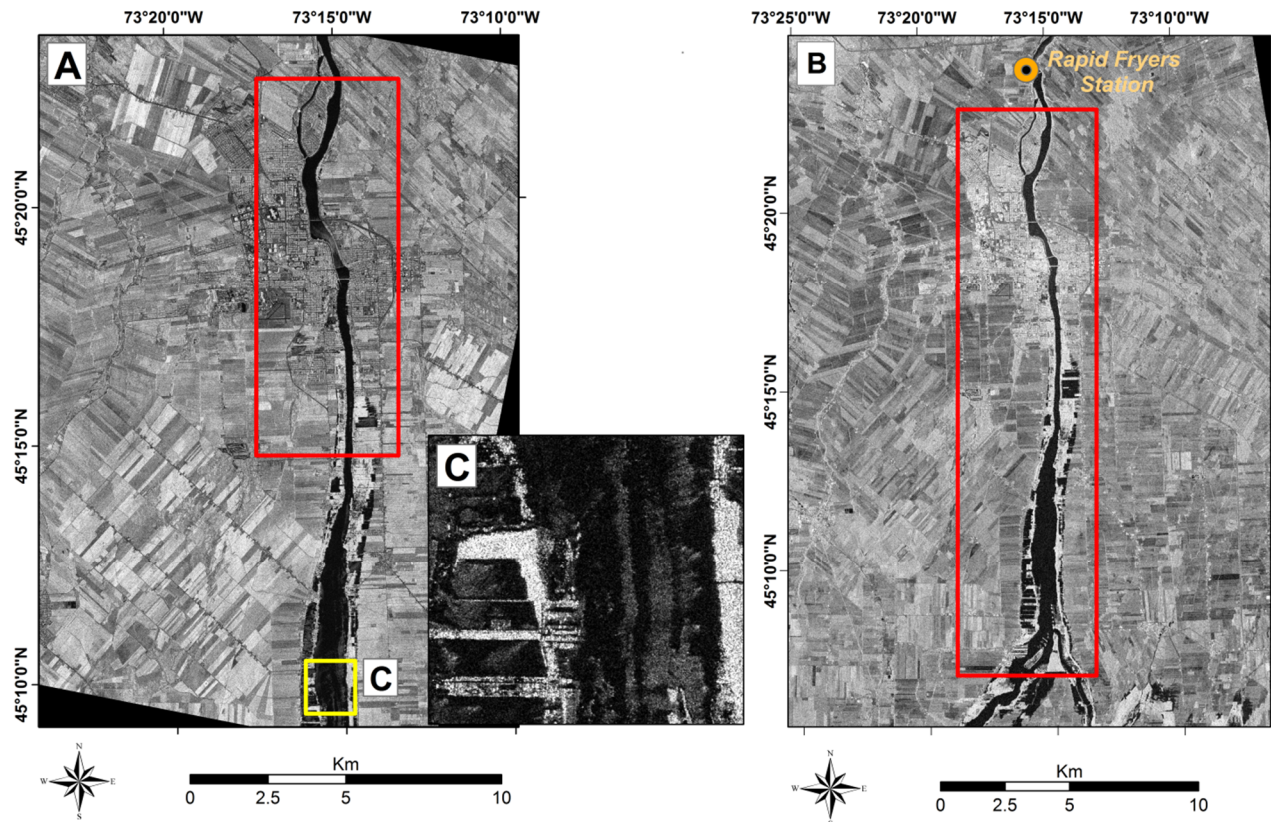
Fig. 4: (A) RADARSAT-2 (HH) Ultra Fine Mode image acquired on May 1, 2011. (B) RADARSAT-2 (HH-HV) Fine Mode image acquired on May 7, 2011; location of the Rapid Fryers gauging station indicated. Red boxes represent the areas covered by the SAR sub-images and by their associated validation data. (C) Open water areas affected by wind disturbance.

To decrease the contribution of speckle, a Gamma-Map filter (Lopes et al., 1993) with a window size of 5 x 5 pixels was applied. This adaptive speckle filter preserves the edges of the features, which is advantageous for the object-oriented segmentation step of the proposed method. To reduce processing time associated with the object-oriented segmentation of the images, subsets of the RADARSAT-2 scenes were created. Each sub-image covers an area identical to that covered by its associated validation data (red boxes in Fig. 4).

464

465   *3.3 Validation dataset*

466

467   Two very-high-resolution multispectral images were used to validate the flood extent maps

468   produced by the algorithm. Their characteristics are summarized in Table 2. On May 1, 2011,

469   the GeoEye-1 satellite overpassed the Richelieu River at 01:09 pm local time during clear-sky

470   conditions, providing pan-sharpened multispectral scenes of the flooded areas with a spatial

471   resolution of 0.6 m. At the time of acquisition, the water level recorded at the Rapid Fryers

472   gauging station was 27.47 m (relative to sea level), identical to the water level recorded at the

473   time of the RADARSAT-2 Ultra-Fine Mode acquisition earlier that day. The limits of the flood

474   should thus be similar in the two scenes. The mosaic of GeoEye-1 scenes covers only a small

475   part of the area imaged by the RADARSAT-2 scene (red box in Fig. 4A). Therefore, validation of

476   the final flood extent map was possible only for a 13.5 km stretch of the Richelieu River.

477   However, despite its reduced size, this section contains a wide range of flooded land cover

478   types, including built-up areas, fields, forested areas, and other vegetation.

479   Table 2: Characteristics of the very-high-resolution multispectral GeoEye-1 and IKONOS-2 pan-

480   sharpened images used to validate RADARSAT-2–derived flood extent maps.

| Reference images for validation	Acquisition Date and Time (local time)	Sensor Mode	Pan-sharpened Spatial Resolution (m)	Cloud Cover (%)	Average Nadir angle (°)
GeoEye-1	May 1, 2011 10:59	PAN/MS1	0.6	0	5
IKONOS-2	May 8, 2011 10:56	PAN/MS1	1	6	9

481

482   The image used to validate the flood extent map generated from the RADARSAT-2 Fine Mode

483   image acquired on May 7, 2011 consists of a mosaic of pan-sharpened IKONOS-2 images with

484   1 m spatial resolution acquired on May 8, 2011 at 10:56 am local time, during almost clear sky

485   conditions (cloud cover <6%). Despite the delay of almost 27 hours between acquisition of the

486   RADARSAT-2 image and that of the IKONOS-2 image, the water levels measured at the Rapid

487   Fryers gauging station were very similar (27.57 m and 27.53 m, respectively). Thus, this delay

488   should not lead to important differences between the SAR-derived flood extent map and the

489   validation map. The mosaic of IKONOS-2 images covers the entire portion of the river that was

490   severely impacted by the flood, enabling us to test the algorithm on a section of the river more

491   than 29.5 km long (red box in Fig. 4B). This section contains large areas of flooded fields and

492   vegetation, and numerous flooded built-up areas.

493   Special care was paid to geocorrection of the pan-sharpened images in order to ensure their

494   precise overlap with the RADARSAT-2 flood images. For both SAR images, sub-pixel precision

495   was achieved. The flood extent was manually delineated on both pan-sharpened images (Fig.

496   5). The very high resolution of these images, minimal cloud cover presence, and linear shape of

497   the study area and of the flooded areas made delineation of the open water rather easy in most

498   locations. However, the delineation task was more complex in urban areas. It was indeed

499   particularly difficult to visually detect, and therefore to delineate, the limit of the flood around

500   each building in residential areas, because of the important presence of garden arrangements

501   and vegetation. Also, the distinction between flooded and unflooded lawns, which colours are

502   rather similar on the pan-sharpened images, was not always obvious. Therefore, decision has

503   been made to consider the buildings around which the limit of the flood could not be clearly

504   seen as flooded, as well as buildings having at least one side in contact with the flood.

505   Conversely, buildings around which the flood could easily be delineated were considered

506   unflooded. Some difficulties also arose during flood delineation inside vegetated areas located

507   along the river, such as woods and wetlands. Most of these areas were entirely flooded due to

508   their close proximity to the river channel, but small areas within them were protected from water,

509   due to higher ground elevations. These small areas are often partially masked by vegetation,

510   and their manual delineation was challenging. Therefore, some of them may have been

511   considered as flooded in the validation datasets. Lastly, the limit between flooded and water-

512   saturated but non-flooded soils was not always obvious in certain flooded fields, and was made

513   more complex by the presence of wind.

514
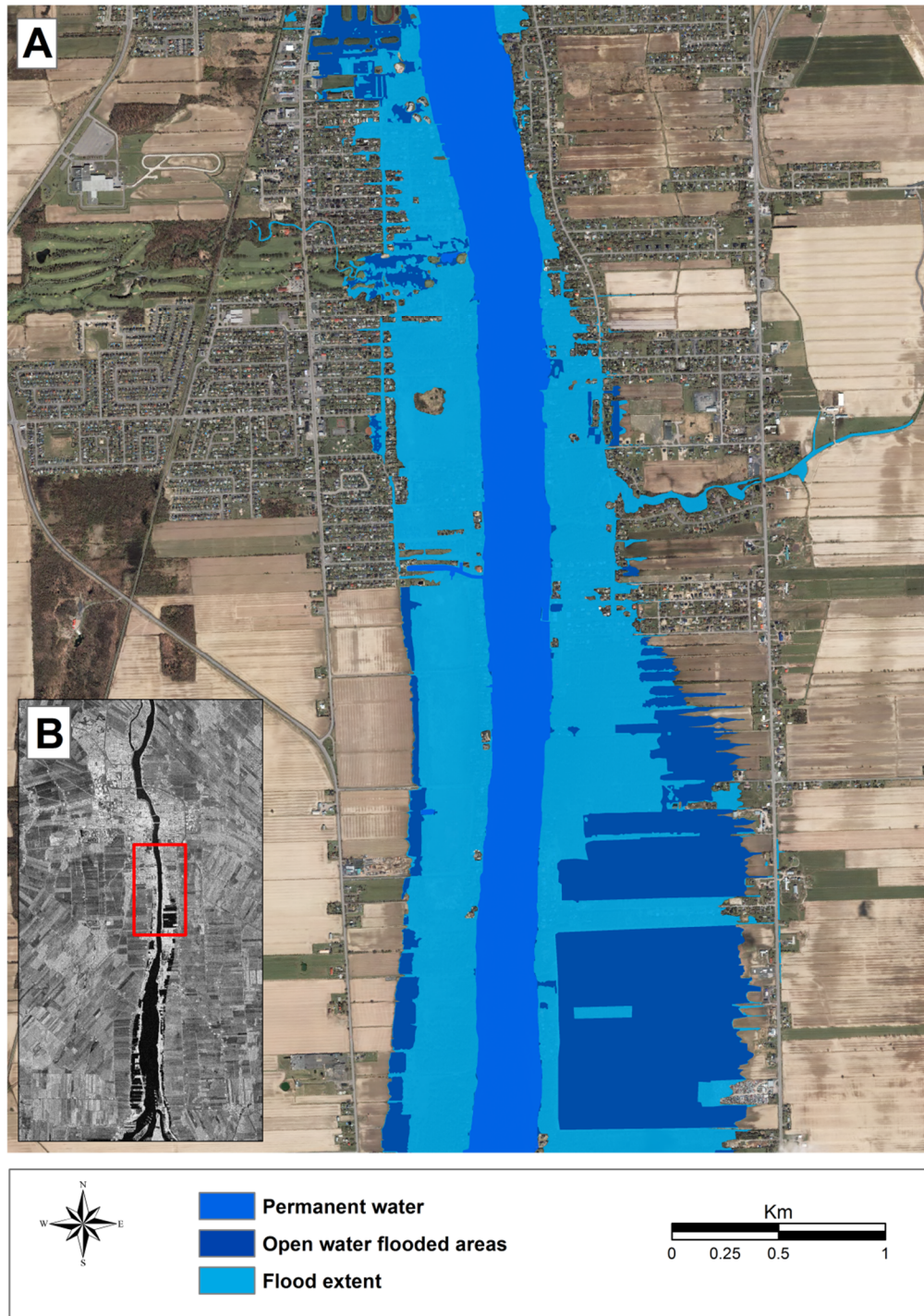
Fig.5: (A) Zoom into the flood validation map obtained from manual delineation on the very-high-

resolution IKONOS-2 image of the Richelieu River acquired on May 8, 2011; (B) Location of the

zoomed area on the RADARSAT-2 Fine Mode flood image acquired on May 7, 2011.

3.4 Flood return period data

The Digital Elevation Model (ground surface elevations) for the Richelieu River basin; the 2-, 20- and 100-year RP shorelines available for the river; and the water heights at the river centreline for each RP were used to produce the flood return period map for the Richelieu River floodplain. The shorelines are polyline features and the water heights at the river centreline are point features, with water height values attached in a geodatabase. The three RP standards used for floodplain mapping in the province of Quebec are 2, 20 and 100 years. These RP shorelines were generated by the Centre d'Expertise Hydrique du Québec (CEHQ), the governmental agency in charge of their production in Quebec. This data, as well as that of more than 600 other river stretches throughout the province, are available on demand from the CEHQ,

The data for the river stretch at study was updated in 2006 by the CEHQ. Data from the Rapid Fryers gauging station (located in Fig. 4) was used to perform the statistical analysis necessary to estimate the discharge associated with each RP (CEHQ, 2006). A Log-Pearson type III distribution was adjusted on 28 annual maximum discharge values recorded at this station between 1972 and 2000 (minimum of 579 m³/s and maximum of 1260 m³/s). The Chi-square goodness of fit test applied to the distribution shows a p-value of 0.0576.

A stage-discharge relation method was used to estimate the water level associated with each RP for 29 sections positioned along the river according to its geomorphological characteristics. Water levels and their simultaneous discharge values were first recorded at each section during several field surveys. Then, stage-discharge relations were defined for four reference sections. Water levels and their simultaneous discharge values were recorded during field surveys, and statistically estimated RP discharge values were used to determine the water levels associated with each RP for these four reference sections. Each reference section was then used to

542   estimate the RP water levels of several upstream or downstream sections. This was done by

543   identifying a stage-stage relation between the water levels recorded at these sections and the

544   water levels recorded at the reference station. This stage-stage relation was used to determine

545   the water level associated with each RP for each section of the Richelieu River. Then, RP water

546   surfaces were generated using an interpolation procedure. Specifically, the HEC-GeoRAS

547   software was used to simulate the RP water surfaces, through Inverse Distance Weighting

548   spatial interpolation of the RP water levels estimated at each section. Ground elevation values

549   were then subtracted from the interpolated water surfaces, to obtain the polygons of RP

550   floodplains, from which the polylines of the floodplain shorelines were derived. These ground

551   elevation values of the area were derived from LIDAR data acquired in 2006 with a point density

552   of 1 point per metre and 0.15 m horizontal and vertical accuracy. Unfortunately, we were not

553   able to obtain information on the accuracy of these RP shorelines.

554   The DEM used in this case study to produce the flood return period map for the river stretch at

555   study is not the one used by the CEHQ for 1D hydraulic modelling. Indeed, LIDAR data

556   acquired in 2006 was limited to a narrow band exceeding the 100-year RP shoreline for a few

557   metres only. It was not appropriate for RP estimation of the points located beyond the 100-year

558   RP shoreline. Therefore, LIDAR data from April 2013, with a point density of 1 point per metre

559   and 0.15 m horizontal and vertical accuracy acquired over the entire Richelieu watershed, was

560   used to produce a DEM for the portion of the river under investigation. The spatial resolution of

561   this DEM, which represents ground surface elevations, was set to 1 m. An analysis of

562   differences in ground elevations between the 2006 and 2013 LIDAR-derived DEMs has shown

563   that these differences are limited. Therefore, the use of this data should not generate major

564   errors in the flood return period map of the Richelieu River floodplain. This map is presented in

565   Fig. 6. Note that the horizontal striations in the south-east of Fig. 6 are caused by the presence

566 of drainage channels which locally decrease the elevation of the ground and therefore change

567 the RP of the cells.
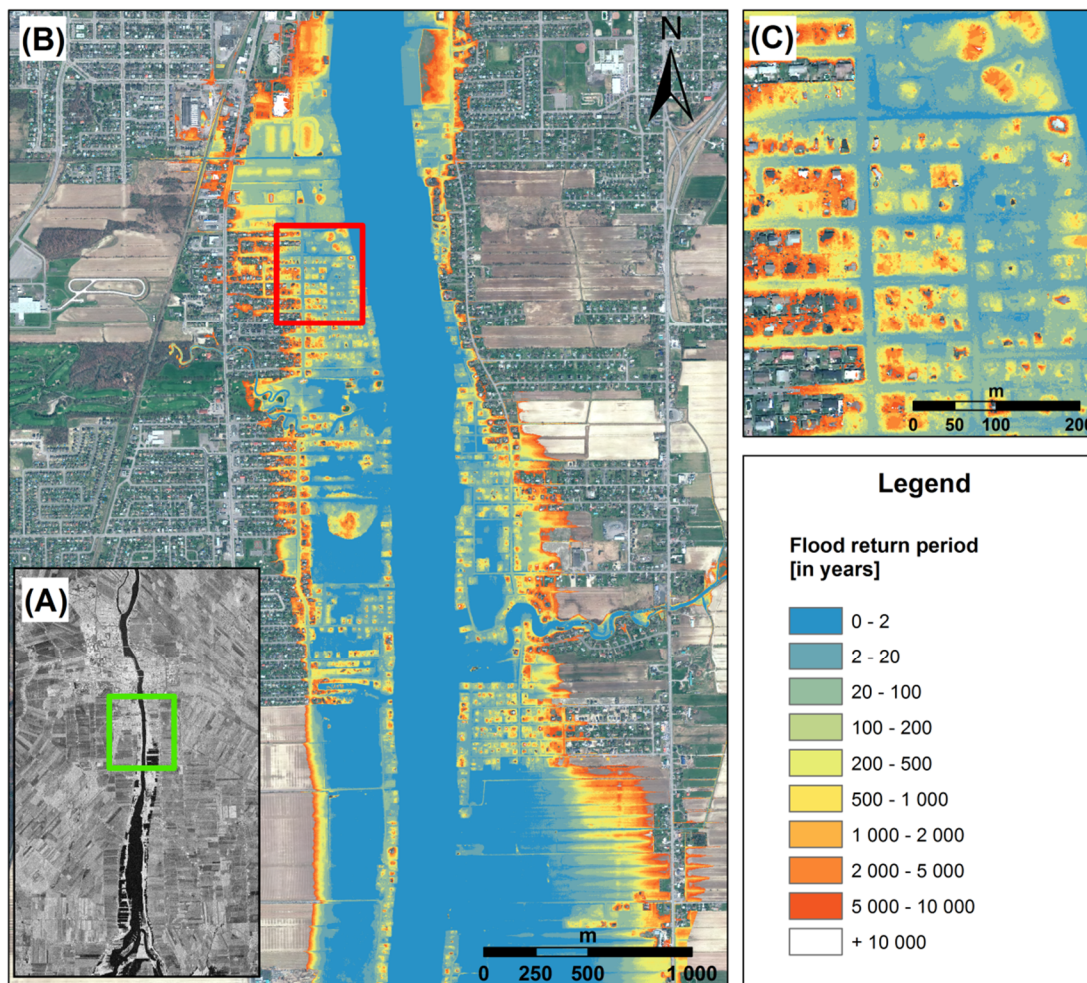
568

569 Fig. 6: (A) Location (green rectangle) on the RADARSAT-2 Fine Mode flood image acquired on

570 May 7, 2011 of the area of interest (red rectangle in panel (B)); (B) Flood return period map of

571 the Richelieu River superimposed on the IKONOS-2 reference image from May 8, 2011

572 (southern part of the city of Saint-Jean-sur-Richelieu depicted). The red rectangle indicates the

573 location of the zoomed area presented in panel (C); (C) Details of the RPs in a section of the

574 urban area.

575

576 **4. Results**

577

578 *4.1 Detection of open water areas*

579

580 Figure 7 displays the optimized gamma PDFs fitted to the empirical image histograms of the

581 RADARSAT-2 Ultra-Fine Mode (Fig. 7A), and RADARSAT-2 Fine Mode (Fig. 7B) image

582 objects, together with the fuzzy thresholds σ_1^0 and σ_2^0 used for the classification of "open water"

583 objects. Table 3 reports the estimated values and standard errors of the k parameter and the

584 fuzzy thresholds σ_1^0 and σ_2^0 for the optimized gamma PDFs for the Ultra-Fine and Fine Mode

585 flood images.

586 The contingency matrices corresponding to the accuracy of the "open water" classification steps

587 are reported in Table 4. The values in the matrices were computed by comparing the number of

588 pixels identified as open water on the optical high-resolution–derived validation maps against

589 the number of pixels contained in the "open water" objects classified by the image processing

590 algorithm. The contingency maps resulting from the final "open water" refined classification are

591 presented in Fig. 8. To enable precise visualization of the classification results, zooms into

592 areas containing under- and over-detection errors are provided.

593 Table 3: Estimated values and standard errors for the k parameters and fuzzy thresholds σ_1^0

594 and σ_2^0 for the optimized gamma PDFs for the RADARSAT-2 Ultra-Fine Mode and Fine Mode

595 flood images.

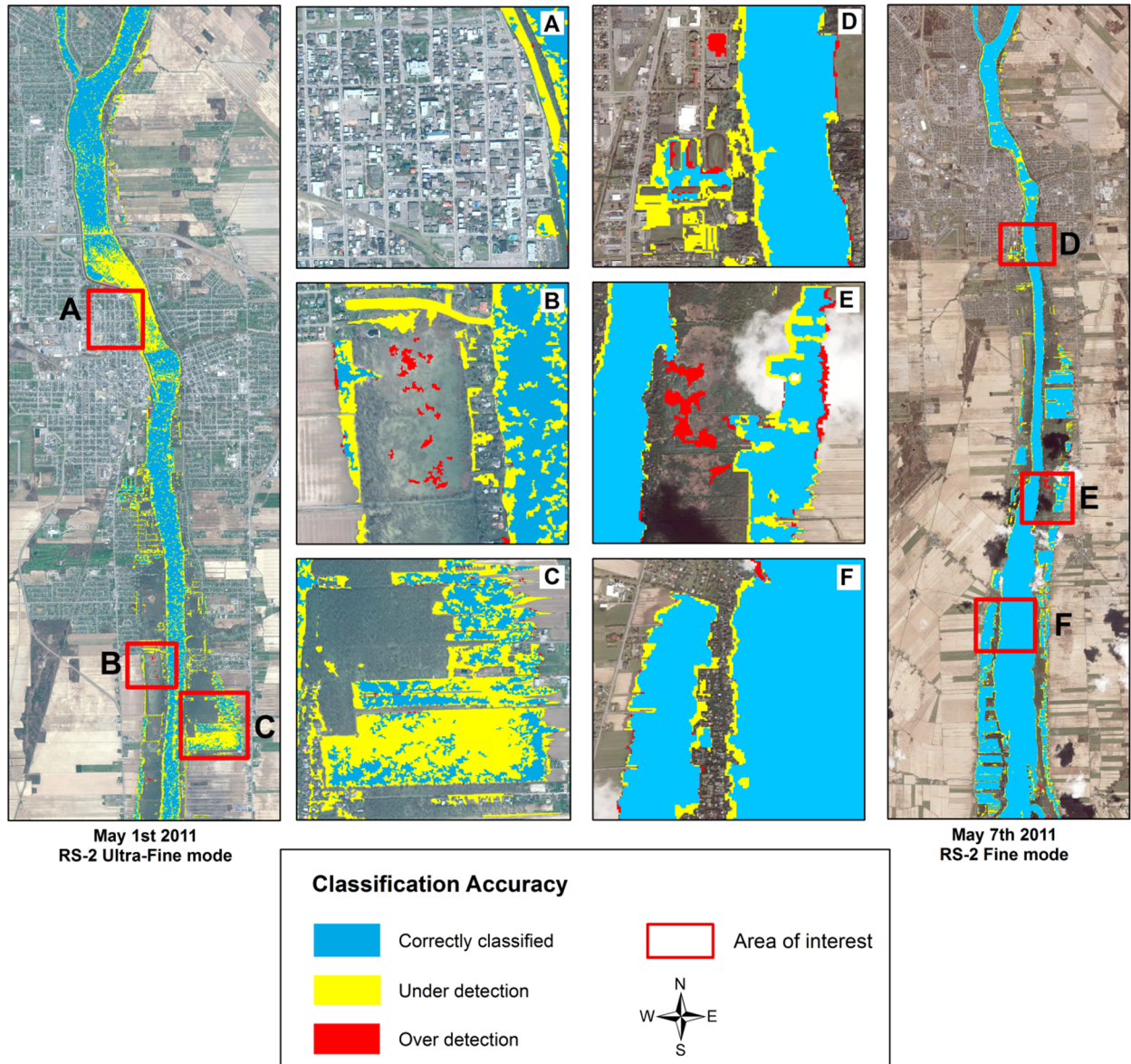|	RADARSAT-2 Ultra-Fine Mode		RADARSAT-2 Fine Mode	
	Estimated Value	Standard Error	Estimated Value	Standard Error
k	0.010	0.008	0.048	0.007
σ_1^0	-20.03 dB	0.057	-21.70 dB	0.012
σ_2^0	-14.76 dB	-	-16.76 dB	-

596

597
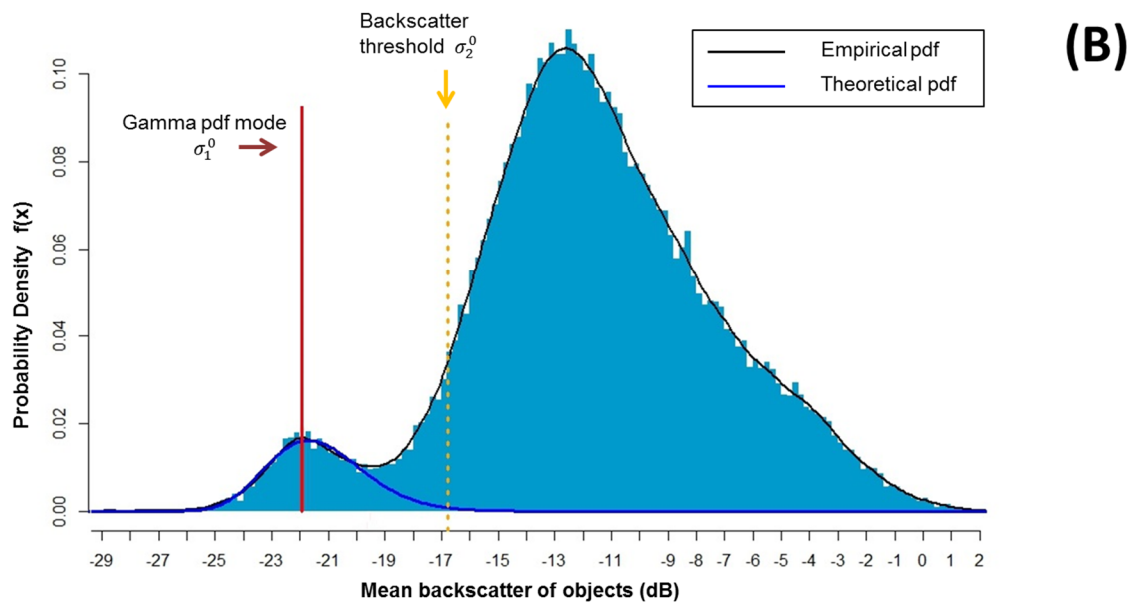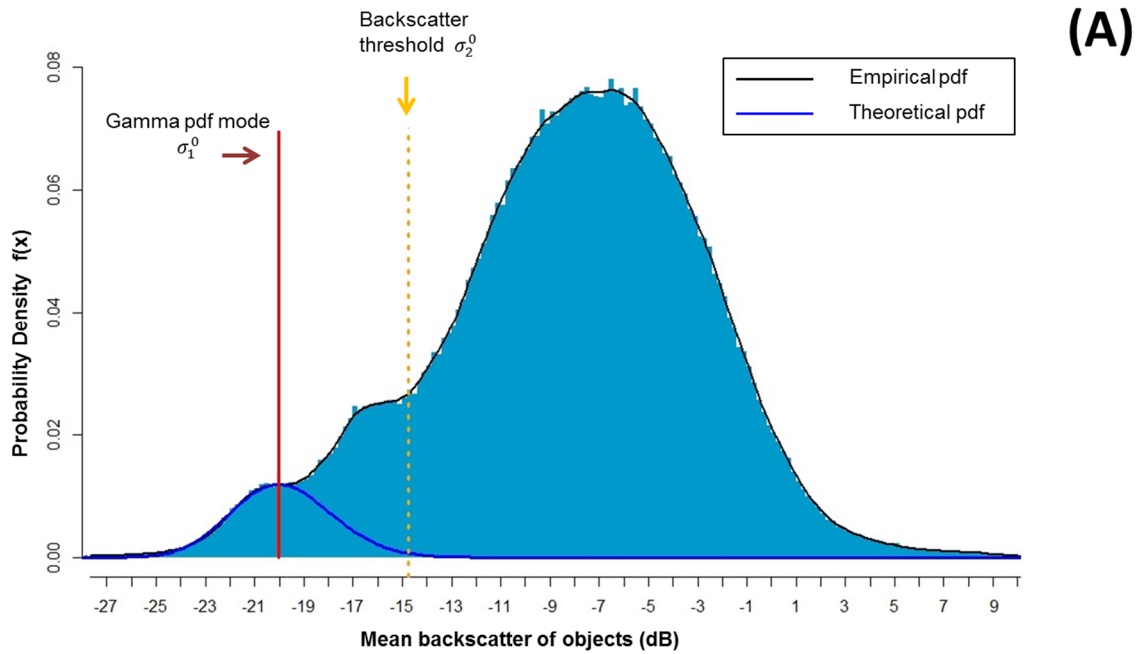
Fig. 7: Optimized gamma PDF superimposed on the empirical image histograms of the RADARSAT-2 Ultra-Fine Mode (panel A) and RADARSAT-2 Fine Mode (panel B) image objects. The fuzzy thresholds σ_1^0 and σ_2^0 used for the classification of "open water" objects are also shown.

602   Table 4: Quantitative evaluations of RADARSAT-2–derived "open water" detections

	Open water classification steps	% correctly classified*	% under detection*	% over detection*
RADARSAT-2 Ultra-Fine Mode	Initial classification	65	35	30
	Refinement using membership degree	64	36	18
	Refinement using RP	64	36	1
RADARSAT-2 Fine Mode	Initial classification	88	12	10
	Refinement using membership degree	87	13	5
	Refinement using RP	87	13	2

* % of pixels identified as open water on the validation data sets

603

Classification Accuracy

Correctly classified — Under detection — Over detection — Area of interest

May 1st 2011
RS-2 Ultra-Fine mode

May 7th 2011
RS-2 Fine mode

604

605 Fig. 8: Contingency maps of the final refined classification of "open water" objects deriving from

606 the application of the method to the RADARSAT-2 Ultra-Fine and Fine Mode flood images.

607

608 *4.1.1 Analysis of "open water" under-detection*

609 From Table 4, it can be observed that the ability of the fuzzy thresholds σ_1^0 and σ_2^0 to correctly

610 classify "open water" objects varies between the two SAR images. While 88% of the flooded

611 pixels were correctly identified on the Fine Mode flood image using these fuzzy thresholds, only

612   65% of the flooded pixels were accurately identified on the Ultra-Fine Mode flood image. The

613   high rate of "open water" under-detection in the Ultra-Fine Mode case study can be explained

614   by the significant presence of waves and ripples on the open water surfaces. This produced an

615   important increase in backscatter values of the "open water" areas and a substantial overlap

616   between mean backscatter values of "open water" and other land-use types. This overlap is

617   particularly obvious when looking at the empirical histogram of the mean backscatter of the

618   objects in the SAR image, displayed in Fig. 7A.

619   The 12% under-detection associated with the RADARSAT-2 Fine Mode "open water" object

620   classification occurred mainly along the borders of inundated fields in rural areas, and along the

621   edges of the main river channel and small tributary rivers (panels D to F in Fig. 8). The

622   difference in spatial resolution between the Fine Mode image and the IKONOS-2 image (the

623   source of the validation data) partly explains this under-detection. However, it is also imputable

624   to the presence of vegetation along the edges of open fields and the river, which tends to

625   increase the SAR signal return due to double-bounce scattering between the soil and the

626   vegetation layers. This effect is also responsible for part of the under-detection on the Ultra-Fine

627   Mode flood image (see panels B and C in Fig. 8). Thus, not all of the under-detection errors are

628   imputable to the image processing algorithm; some result from the inherent limitations of the

629   SAR C-Band imaging technique.

630   According to Matgen et al. (2011), backscatter values between -24 dB and -10 dB can be

631   considered appropriate for open water pixels for most currently available sensors. Analysis of

632   the backscatter values of the under-detected "open water" pixels in the two case studies shows

633   that many pixels with backscatter values typical of open water were excluded from the "open

634   water" classification because they belonged to objects with mean backscatter values that were

635   higher than the fuzzy membership degree defined for open water (see Fig. 9). Thus, in spite of

636   the attention that was paid to the selection of optimal parameter values for the multi-resolution

637   segmentation procedure, image segmentation inaccuracies remained locally present. However,

638   the impact of these inaccuracies on the classification results was moderate, as they were

639   responsible for only 4% and 0.4% of the under-detections on the Ultra-Fine Mode and Fine

640   Mode images, respectively.
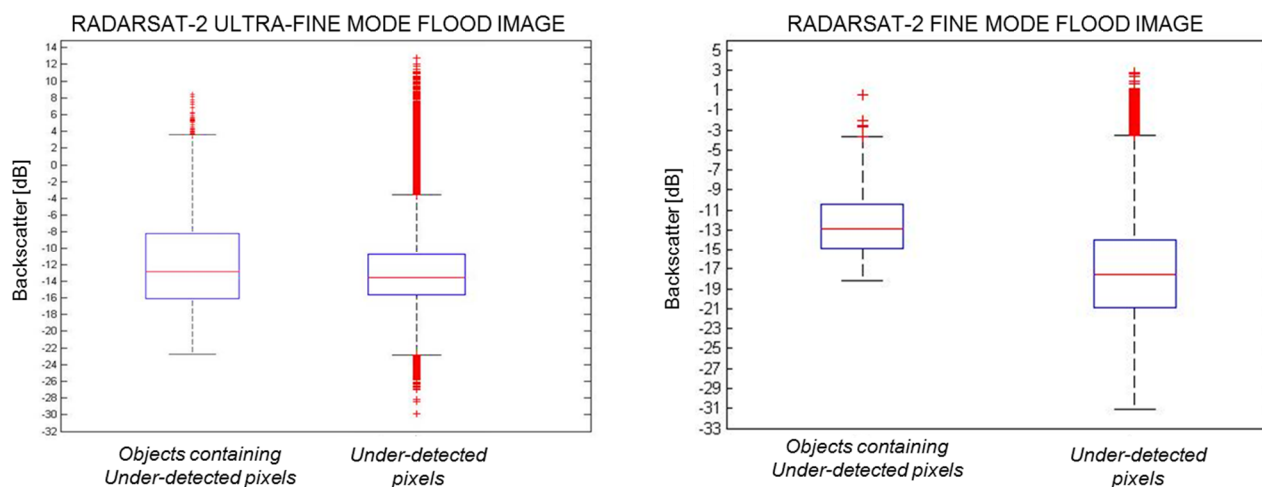
641

642   Fig. 9: Boxplot of the mean backscatter values of objects containing under-detected "open

643   water" pixels, and the backscatter values of under-detected pixels, for the Ultra-Fine Mode and

644   Fine Mode flood images.

645

646   *4.1.2 Analysis of "open water" over-detection*

647   Most of the over-detections in the initial "open water" classification on the Ultra-Fine Mode

648   image were located in urban areas, on unflooded surfaces characterized by specular-like

649   reflection, such as roads parallel to the orbit track and parking lots; areas affected by the

650   shadow effect were also a source of over-detections. Conversely, on the Fine Mode image,

651   which did not have sufficient spatial resolution to detect such fine-scale urban elements, the

652   over-detections were located in rural areas, on bare, smooth fields. These errors can be

653 explained by the high soil moisture at the time the image was acquired, which resulted in low

654 backscatter values from bare soils (Ulaby et al., 1986).

655 In both case studies, the benefit of using both the objects' membership degree in the "open

656 water" class and the RP data to refine the "open water" classification is obvious, with large

657 decreases produced in the rates of "open water" over-detection (see Table 4). Classification

658 refinement based solely on the membership degree of objects enables a significant reduction in

659 over-detections, but at rates that cannot guarantee extraction of an accurate RP for flood extent

660 mapping in urban and rural areas. Classification refinement based on the classified objects' RP

661 is thus also essential. For information purposes, the RPs used for "open water" classification are

662 of 609 years in the Ultra-Fine mode case study and of 540 years in the Fine mode case study.

663 As shown in Table 4, the over-detections of "open water" areas were reduced to 2% for the Fine

664 Mode image and to 1% for the Ultra-Fine Mode image. In both case studies, the decrease in

665 classification accuracy associated with the classification refinement was only 1%. Therefore,

666 and as presumed in section 2.5, the use of the objects' membership value and their spatial

667 connection to objects with a high membership degree in the "open water" class does not result

668 in the inclusion of objects containing hedgerows or wind-affected water surfaces in the "open

669 water" class. This tends to validate the "superior or equal to 0.5" membership degree rule and

670 the use of RPs for refining the "open water" classification.

671 After these two classification refinement steps, most of the remaining over-detection is located

672 at the upper boundaries of the flooded fields and in vegetated flooded areas (see panels B, E,

673 and F in Fig. 8). Over-detection at the upper boundaries of the flooded fields was more

674 important in the Fine Mode image case study than in the Ultra-Fine Mode case study. Again,

675 this can be related to the difference between the spatial resolution of the Fine Mode image and

676 the IKONOS-2 scene used as evidence of the flooding extent. An additional factor is that the

677 flood was receding by the time these images were acquired, and visually distinguishing between

678   the water-saturated soils and the flooded soils was locally laborious at the extremities of open

679   water areas. This may have led to local inaccuracies in the IKONOS-2–derived validation flood

680   map.

681   The remaining over-detections due to specular backscatter from unflooded areas (parking lots,

682   shadow areas around buildings, etc.) were trivial in both case studies. Only one non-flooded

683   parking lot located beside the river was classified as "open water" on the Fine Mode flood image

684   (see Fig. 8D), while no error of this type is to be found on the Ultra-Fine Mode image (see Fig.

685   8A). These results demonstrate the very good capacity of the proposed method to deal with

686   such areas, which are considered a significant impediment to precise flood detection in urban

687   areas using high-resolution SAR imagery.

688   Most of the under-detections were caused by the presence of wind on water surfaces or by

689   double bounces from vegetation. Thus, modification of the fuzzy threshold σ_2^0 toward higher

690   backscatter values would not result in a significant reduction of under-detections and would

691   come at the cost of increased over-detections of "open water" areas. Conversely, modification of

692   the fuzzy threshold towards a lower percentile of the gamma distributions would reduce over-

693   detection, but it would also result in increased under-detections of open water areas.

694

695   4.2 Accuracy of flood mapping in urban and rural areas

696

697   The maximum RP extracted from the "open water" classification was 186 years for the

698   RADARSAT-2 Ultra-Fine Mode flood image and 219 years for the RADARSAT-2 Fine Mode

699   flood image. These RPs are not and should not be considered representative of the actual RP

700   corresponding to the discharges or to the water levels registered at the gauging station at the

701   time of the SAR image acquisitions. They should rather be considered indicators related to the

702　maximum extent of the flooded areas identified with certainty, enabling identification of the

703　flooding status of the floodplain cells with inferior or equal RP values.

704　For each case study, the accuracy of the flood extent map that resulted from application of the

705　extracted RP across the entire floodplain is reported in the contingency matrices shown in Table

706　5. The values of the contingency matrices were computed by comparing the number of pixels

707　identified as flooded on the validation maps to the number of pixels classified as flooded in the

708　flood extent maps. The results are considered separately for urban and rural areas, which were

709　distinguished using 1:20 000 scale land cover data provided by the Canadian National

710　Topographic Data Base (NRC, 2015). To enable qualitative evaluation of the method's

711　performance, the results are displayed as contingency maps in Fig. 10.

712　Table 5: Quantitative evaluation of the RADARSAT-2–derived flood extent maps in urban and

713　rural areas

	Area types	% correctly classified*	% under-detection*	% over-detection*
RADARSAT-2 Ultra-Fine Mode	Urban flooded areas	86	14	13
	Rural flooded areas	97	3	35
RADARSAT-2 Fine Mode	Urban flooded areas	87	13	14
	Rural flooded areas	98	2	3
% of pixels identified as flooded on the validation data sets				

714
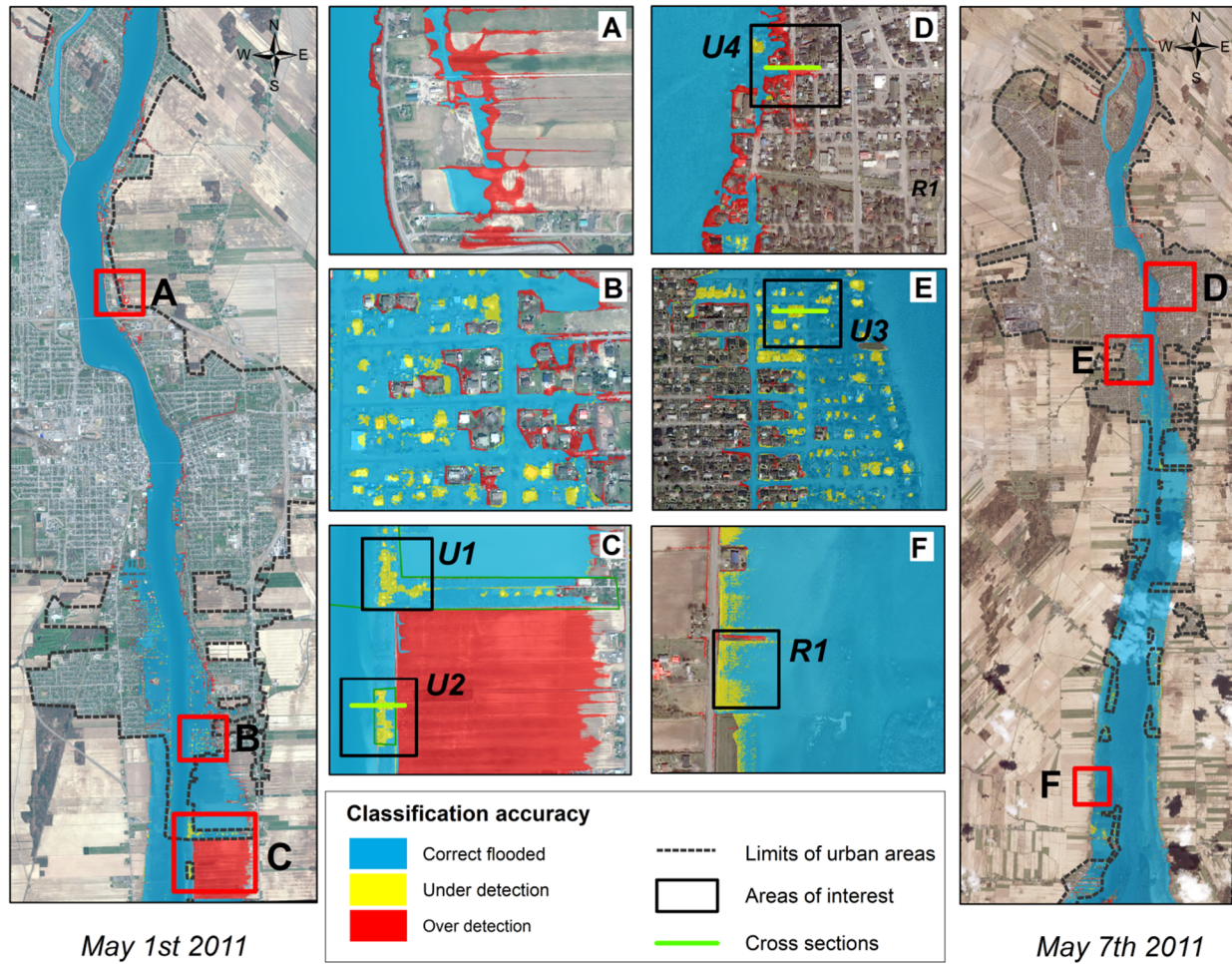
Fig. 10: Contingency maps of the final flood extent maps in urban and rural areas. The left-hand panel shows the contingency map for the May 1, 2011, case study superimposed on the GeoEye-1 image, with zooms into areas of interest shown in panels A, B, and C. The right-hand panel shows the contingency map for the May 7, 2011, case study superimposed on the IKONOS-2 image, with zooms into areas of interest shown in panels D, E, and F.

From Table 5, it can be seen that 86% and 97% of the flooded pixels were correctly identified in the urban and rural areas, respectively, in the May 1, 2011, case study. The extraction of a RP allowing urban and rural flooded areas to be precisely mapped was unlikely, as the rate of correctly detected open water flooded areas was low on the Ultra-Fine Mode image. However, the combination of accurate detection of most "open water" objects located at the outer

41

726   boundaries of open water flooded areas (Fig. 8) and a low rate of open water over-estimations

727   enabled extraction of an accurate RP. The associated over-detection was 13% in urban areas

728   and 35% in rural areas. The causes of this high rate of over-detection will be analyzed in detail

729   in a following section. The results obtained in the May 7, 2011, case study were almost

730   identical, although the "open water" objects classification was significantly better: 87% of the

731   urban flooded pixels and 97% of the rural flooded pixels were correctly identified by the

732   algorithm. The associated over-detection was 14% in the urban areas and 3% in the rural areas.

733   This first overview of the flood extent mapping results suggests that accurate classification of all

734   "open water" objects on a SAR flood image is not strictly required to extract RP values precise

735   enough for flood extent mapping needs. SAR flood images that include water surfaces

736   roughened by wind can thus be used as inputs to this method.

737

738   *4.2.1 Analysis of under-estimations of flooding extent*

739   From Fig. 10C, one can see that two flooded residential areas (labelled U1 and U2) located by

740   the riverside were classified as unflooded by the algorithm in the two case studies. The analysis

741   of the RP of the cells located in these two areas revealed values two to eight times higher

742   (between 2,000 years and 16,000 years) than the RP used for flood extent mapping in the two

743   case studies. These over-estimations of the RP had two sources. First, due to the very similar

744   elevations of the 20-year and 100-year floodplain limits in these areas, the differences between

745   the 20-year and 100-year RP water surface elevations were very low. Therefore, small

746   variations in ground surface elevation resulted in very large increases in RP, as shown in Fig.

747   11A. Also, it can be seen that the 20-year RP water surface has higher local elevations than the

748   100-year RP water surface, which results in important inaccuracies in the RP estimates (Fig.

749   11A). This error is due to the fact that the elevation points along the 100-year RP shoreline used

750   for interpolation of the associated water surface were less numerous and were unequally

751   spatially distributed in these two areas, unlike the points used for interpolation of the 20-year RP

752   water surface. This lent greater influence to more distant points in the interpolation of the 100-

753   year RP water surface, leading to local inaccuracies in water surface elevations.

754   The aforementioned errors only concern a moderate proportion of the overall under-detections

755   in the urban areas. Most of the under-detections in the urban areas are located around

756   buildings, and form small individual areas (Fig. 10B and Fig. 10E). The analysis of ground

757   elevations in these areas revealed slight increases around the buildings, which results in RP

758   increases. To illustrate this phenomenon, an example extracted from the area identified as U3 in

759   Fig. 10E is provided in Fig. 11B. These increases in ground elevations around buildings are

760   typical of the presence of basements, which seems to have prevented the buildings from being

761   flooded. Considering the difficulties associated with manual delineation of the flooding around

762   each building, it appears that these under-detections reveal the presence of zones that were

763   actually non-flooded. This underlines the ability of the method to precisely define the flooding

764   status of most of the buildings in urban areas as long as high-resolution, high-precision

765   elevation data are available for the production of the RP map. Finally, in both case studies,

766   under-detection was very low in rural areas, and was concentrated at the upper boundaries of

767   flooded fields (Fig. 10F). Errors in the validation maps can explain such inaccuracies, as flooded

768   and water-saturated but non-flooded soils were often difficult to distinguish in these areas.

769

770
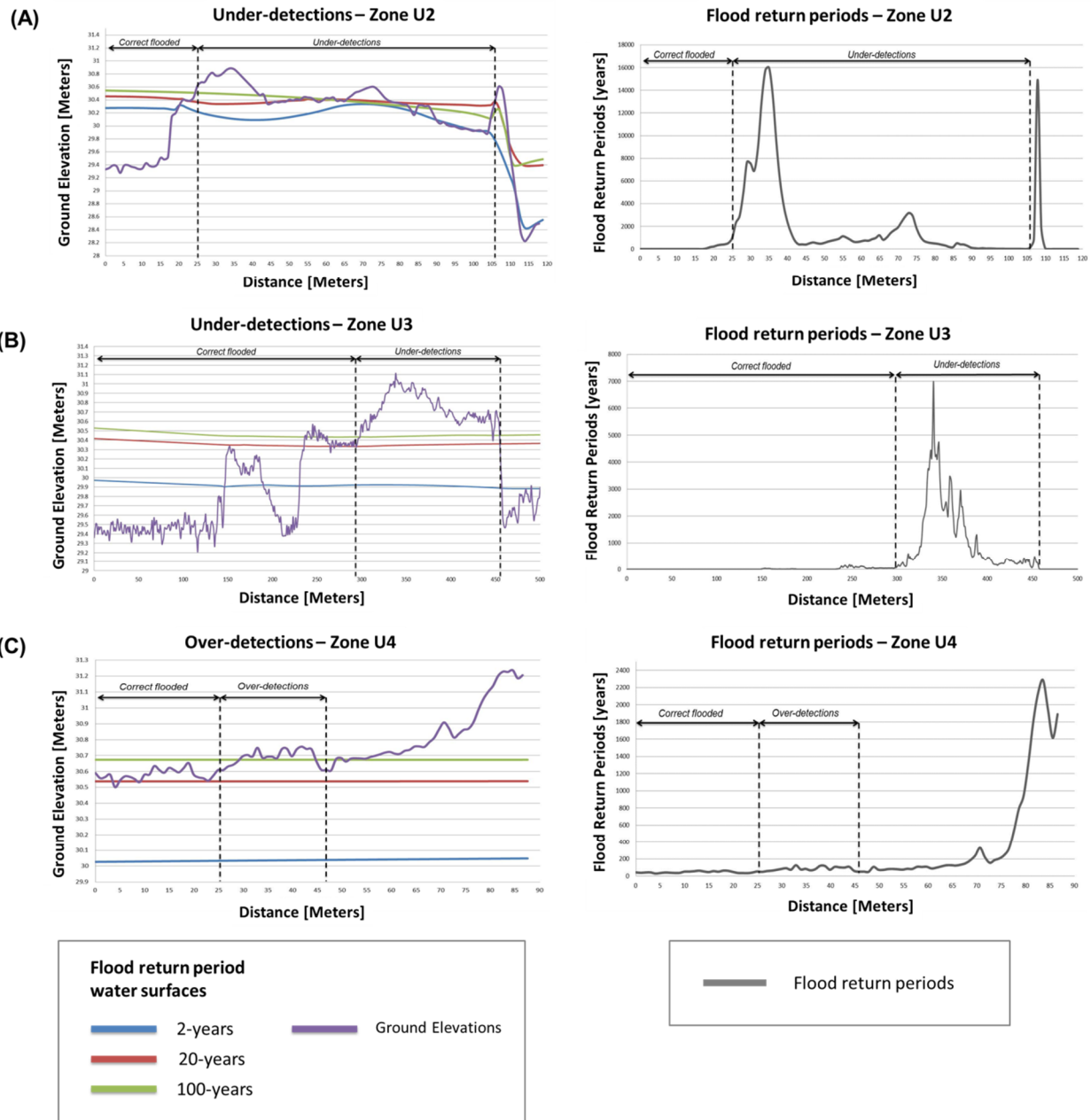
Fig. 11: Analysis of flood extent mapping under-detection (panels A and B) and over-detection (panel C) for different zones of the study area. The left panels allow the analysis of the values and the spatial tendencies of the ground elevations and of the water surfaces elevations in areas where flood mapping inaccuracies were located. The right panels allow the analysis of the values and of the spatial tendencies of the RPs in these areas.

4.2.2 Analysis of over-estimations of flooding extent

A very large proportion (88%) of the over-estimations in rural areas of the May 1 case study was due to misclassification of a single unflooded field located in the southern part of the study area (Fig. 10C). Insofar as the 2-year RP floodplain limit is located in the middle of this field and the surrounding fields were almost entirely flooded on this date, it was reasonable to expect that this field should also be flooded. Indeed, the IKONOS-2 image shows that it was almost entirely flooded six days later, on May 7. A thorough visual analysis of the GeoEye-1 scene reveals that, on May 1, work was being conducted on the embankment that surrounds three of the four sides of this field. In the later IKONOS-2 scene, two large breaches that were not visible on the GeoEye-1 image are present in the embankment, enabling the water to flood the field. It appears that an attempt to reinforce the embankment was made during the rising phase of the flood in order to protect the field and habitations located on its eastern side, but that these mitigation efforts were ultimately unable to withstand the water level rise.

The remaining over-estimations are mainly located at the urban and rural flooded area edges, and are connected. Two examples of flood extent over-estimations are displayed in Fig. 10A and Fig. 10D. Both are located in areas where the ground surface elevation gently varies but stays close to the elevation of the 100-year RP water surface. Thus, the RP does not undergo significant variation and remains low, within a range of values that does not exceed 200 years. This phenomenon can clearly be seen in Fig. 11C. In such cases, over-estimation by just a few years of the RP extracted from the objects classified as "open water" on the SAR flood image can lead to over-estimation of the maximum flood extent. This phenomenon is common when considering water levels above bankfull stage, in large and rather flat floodplains such as the Richelieu river floodplain, and should therefore be frequently observed. Conversely, in floodplains with more pronounced topography, a small increase of water level should lead to a small increase of the flooded area, and therefore to less abrupt increases in RP. The presence

803 of connected areas of over-estimation along the edges of the correctly identified flooded areas

804 indicates that this method for extracting the RP from the objects classified as "open water" on

805 the SAR image tends to slightly over-estimate the RP. However, the resulting over-estimations

806 remain low and should not lead to major issues in terms of flood crisis management.

807

808 **5. Discussion**

809

810 Despite some local inaccuracies, mostly due to errors in the RP estimated for each point of the

811 floodplain, the method presented here enabled correct identification of the flooding status of

812 most pixels in the areas of interest in both May 1 and May 7, 2011 Richelieu River flood case

813 studies. These initial results show the consistency of this innovative method and demonstrate

814 that it competes well with existing algorithms in terms of urban and rural flood extent mapping

815 precision. Indeed, from Table 6, which reports the results of urban and/or rural flood extent

816 mapping obtained with other methods, it can be seen that best urban flood mapping accuracy

817 reported to date was obtained by Giustarini et al. (2013), who correctly identified around 82% of

818 urban water pixels on a TerraSAR-X flood image acquired in HH polarization mode. Rural flood

819 extent mapping was not considered in that study. However, in cases such as the Richelieu River

820 flood, accurate rural flood extent mapping is also essential, as many small rural residential

821 areas and private cottages located on the riverside are at high risk of flooding and may end up

822 isolated because their access roads are exposed to flooding. To our knowledge, the best flood

823 detection accuracy in rural areas was obtained by an algorithm developed by Martinis et al.

824 (2009), which proved capable of detecting $\sim$ 95% of rural flooded pixels on a TerraSAR-X

825 image with an associated false positive rate of 1% (see Table 6). According to the authors, the

826 algorithm does not perform well in urban areas, and is affected by double bounce effect, side-

827 lobes strong reflectors etc.

828 Table 6: Summary of relevant research conducted in SAR-based urban and rural flood extent

829 mapping. In the "Key results" column, code (1) refers to urban flood mapping accuracy; (2) rural

830 flood mapping accuracy; (3) key aspects of the method or of the results.

Study	Data used	Approach	Key results
1. Matgen et al. 2011	ENVISAT & RADARSAT-1 /	Automated histogram thresholding, combined with region growing algorithm	Change detection is included as an additional step that limits over-detection of inundated areas, but results show that considering pre- or post- flood image gives the same performances as optimized manual approaches. 84.5% of pixels correctly detected in rural areas, 6% over-detection, 9.6% under-detection. Urban areas not analyzed
2. Guistarini et al. 2013	TerraSAR-X	Backscatter thresholding combined with region growing and change detection	Areas in shadow and with permanent water surface-like radar response are masked from the final flood map, to reduce over-detections. 82% of pixels correctly detected in urban areas, 2.6% over-detections, 15.6% under-detections. Rural areas not analyzed
3. Martinis et al. 2009	TerraSAR-X	Tile-based automatic thresholding approaches, and refinement using topography	Algorithm performs very well in rural areas, with an overall accuracy of ~ 95%, 1% over-detections and 4% under-detections. Does not perform well in urban areas, due to double bound effects, side-lobes strong reflectors etc.
4. Martinis et al. 2011	TerraSAR-X	Change detection using Tile-based parametric thresholding applied on a normalized change index data, combined with Markov image modeling	Integration of spatial-contextual information in the classification using noncausal Markov Random Field modelling increases classification accuracy. Experimental results confirm the effectiveness of the approach, with an overall error of ~7.5% (~92.5% classification accuracy). Urban and rural areas are not differentiated.
5. Mason et al. 2010	TerraSAR-X	Snakes conditioned by SAR and LIDAR data in rural areas; Region growing guided by rural flood heights in urban areas	Areas of radar shadow and layover are estimated using a SAR end-to-end simulator and LIDAR data, and are masked out in the processing stages. 76% of flooded pixels correctly detected in urban areas, 25% over-detections, 24% under-detections. If all urban water pixels are considered, results fell to 58% of correctly detected pixels with an associated positive rate of 19%.
6. Mason et al. 2012	TerraSAR-X	Image segmentation combined with thresholding-based classification for urban areas; Region growing guided by rural flood heights in urban areas.	Areas of radar shadow and layover are estimated using a SAR end-to-end simulator and LIDAR data, and are masked out in the processing stages. 89% of pixels correctly detected in rural areas, 6% over-detections, 11% under-detections 75% of pixels correctly detected in urban areas, 24% over-detections, 25% under-detections. If all urban water pixels are considered, results fell to 57% of correctly detected pixels with an associated positive rate of 18%.

7. Mason et al. 2014	TerraSAR-X	Estimation of double scattering strengths using a SAR image and a high resolution LIDAR data height map	Observations of double scattering strengths compared with predictions from an electromagnetic scattering model. Successful detection of double scattering curves due to flooding in a single-image case (100% classification accuracy) and of un-flooded curves (91% classification accuracy). Same figures achieved using change detection between flooded and un-flooded images.
8. Pierdicca et al. 2008	ERS-1	Fuzzy-based classification, integration of SAR measurements and of land-cover map for backscatter analysis, and of DEM to include simple hydraulic considerations	Use of land cover information and of simple hydraulic consideration derived from DEM data helps at improving open water detection. Urban and rural areas are not differentiated. 87% of correctly detected pixels, 5% over- detections and 8% under-detections.
9. Pulvirenti et al. 2015	COSMO-SkyMed	Analysis of coherence data and of intensity data trends, coupled with manual classification and a region growing technique	First successful attempt to detect flood in urban areas using inSAR theory. Visual analysis of results and analysis of coherence and intensity data trends. Multi-temporal trend of Coherence useful for the interpretation of SAR data and fundamental to reduce omission errors. Post-event coherence useful to observe the persistence of water. Interferometric data helps distinguishing zones where water receded from areas where it persisted for a longer time.
10. Chini et al. 2012	COSMO-SkyMed	Complex coherence and intensity information combined in a RGB composite image, followed by visual interpretation	Visual interpretation of the RGB color composite image and validation using a couple of optical images used as benchmarks. The high resolution of the images used (3m) and the interferometric coherence underline the presence of flood water in urbanized areas. The temporal analysis of intensity information allows detecting rural flooded areas, receding of flood water and moving of debris along the flooded fields.
11. Tanguy et al.	RADARSAT-2	Combination of SAR-based open water detection and of RP data	First successful attempt to combine SAR data and RP data for urban flood mapping. In urban area, ~ 87% of pixels correctly identified, with under-and over-detections ~ 14%. In rural areas, 97% of flooded pixels correctly identified, with under-detection ~ 3% and over-detection between 3% and 35%.

831

832

833 The method presented by Guistarini et al. (2013) seeks to minimize the risk of flood extent over-

834 detections by masking permanent smooth areas from the final flood map. A similar technique

835 has also been used by Mason et al. (2010, 2012) to mask areas affected by shadow and

836 layover effects. In both cases, the mask covered a significant part of the area of interest ~20%

837 in Guistarini et al. (2013) and 39% in Mason et al. (2012), which means that the flooding status

838 of a non-negligible part of the urban areas was not identified. By contrast, the method presented

48

839   here does not require such masks, and seeks to detect water pixels in urban areas using

840   hydraulic data and topography. The final results of this method are not affected by permanent

841   water surface-like radar response areas or layover and have the advantage of considering all

842   the pixels of the area of interest in the flood extent maps. From Table 6, it can also be seen that

843   combined intensity and coherence information analysis methods presented by Chini et al.

844   (2012) and Pulvirenti et al. (2015) also appear promising. However, in the absence of

845   quantitative information about the precision of these methods, it is not possible to compare their

846   performance to the one hereby presented. Both methods rely on the availability of SAR

847   interferometric pairs to analyze multi-temporal trends of coherence information, which may limit

848   their wide application. However, future improvements in satellite constellations like Sentinel

849   (ESA) and RADARSAT should provide users with more useful data.

850   The availability issue of the aforementioned data highlights one of the limits of the method

851   presented here. A recent report by Public Safety Canada (Public Safety Canada, 2014)

852   confirmed that the RP shorelines required by the method are available for most rivers equipped

853   with hydrometric gauging stations in several countries, such as Canada, UK, USA, France,

854   Germany, Switzerland, Australia and New Zealand. The proposed approach should thus be

855   transferable to a very large number of rivers prone to flooding. However, we are aware that

856   these data are not available for all the rivers in the world, especially for those not equipped with

857   hydrometric gauging stations. Therefore, in some cases, the method will not be applicable.

858   Analysis of the over-estimations of flooding extent, section 4.2.2, has also underlined the

859   necessity to use recent or up-to-date RP shorelines to minimize flood extent mapping errors due

860   to land-use and land-cover changes. As the example given in section 4.2.2 demonstrates, local

861   modifications of ground elevations or recent developments that may have an impact on water

862   flow, such as embankments or walls, can't be taken into account by the method for RP

863   estimation at each point of the floodplain. If they have not been integrated into the RP

864   shorelines, they will lead to inaccurate RP estimations and therefore to significant errors of the

865   flood extent maps. The use of recent and up-to-date data is thus strongly recommended, but it

866   is obvious that RP shorelines and topographic height data are not updated yearly. Therefore,

867   the user should check if developments or activities leading to modifications of the ground

868   elevations took place in the area after RP shorelines definition, in order to ensure that the flood

869   extent map will be relevant. In the same vein, the effects of temporary measures to protect

870   buildings and streets, such as sand bags or mobile dams, cannot be accounted for by this

871   method. The impact of such measures on subsequent flooding is restricted to small areas, but it

872   may cause local over-estimations of the extent of the flooding.

873   In the case studies presented here, the availability of RP shorelines generated by using very

874   high horizontal and vertical accuracy LIDAR-derived DEM elevations has enabled us to produce

875   coherent RP estimates at each point of the floodplain and precise flood mapping in both urban

876   and rural environments, with fine-scale details. The use of very high accuracy LIDAR data such

877   as the one exploited in this study (15 cm vertical accuracy and 1 m horizontal accuracy) is

878   recommended with this method. This type of data is increasingly available in some countries

879   such as Canada, although they are not available for all flood-prone areas and are still rare in

880   some countries. The use of low quality, coarser-resolution DEM elevations data (i.e 10 m or

881   20 m resolution) makes hydraulic modelling less efficient at replicating flow processes and

882   reduces its relative accuracy (Jarihani et al., 2015). It leads to less precise RP shoreline

883   estimations, and therefore to less coherent RP estimates at each point of the floodplain. Even if

884   this point has not been demonstrated here with a tangible example, it should be clear that the

885   use of coarser-resolution DEM data will result in less precise urban and rural flood extent maps.

886   It is also worth underlining that the estimation of RPs and shoreline position can be affected by

887   errors and uncertainties from different sources (number and quality of hydrologic observations

888   used for RP estimation, quality of the data used for hydraulic model construction, structural

889   modeling assumptions, etc.). An interesting aspect of the method hereby proposed is that

890   remotely sensed open water areas constrain RPs derived from hydraulic modeling and help

891   reducing uncertainties related to model predictions. To illustrate this point, we offer an example

892   from the 2011 river Richelieu flooding. The statistical analysis used to estimate the RPs of the

893   river section under study has been based on 28 annual maximum river flows registered between

894   1973 and 2000 (see section 3.4). The highest annual maximum flow included in the frequency

895   analysis was of 1260 $m^3.s^{-1}$, whereas the maximum discharge registered on May 7 was of

896   1530 $m^3.s^{-1}$. According to the results of the statistical analysis, the RP corresponding to this

897   discharge is of almost 10,000 years. Using this RP alone to map urban and rural flooded areas

898   may have caused important over-estimations of the flooding extent. This over-estimation has

899   been estimated to be of 52% in urban areas and 20% in rural areas. This example tends to

900   confirm the relevance of combining SAR-derived open water information and RP data for

901   precise flood extent mapping.

902   However, it may happen that the rainfall pattern of the extreme event being studied differs from

903   the rainfall pattern in the catchment integrated to the hydraulic model when defining the flood

904   return period shorelines. For instance, this phenomenon may occur when considering the

905   flooding of a town at the confluence of two rivers. The pattern of flooding in this town will

906   probably be different if one river is flooded rather than the other, due to greater-than-normal

907   rainfalls over one river catchment and not over the other. In that case, the flood map

908   constructed from the maximum RP extracted from SAR-derived open water areas will be in

909   error, and will tend to overestimate the flooding extent on one side of the town. Also, the method

910   presented in this paper does not account for the temporal aspect of flood spread over the

911   floodplain or for the potential presence of areas where water is naturally retained after a

912   decrease in the water flow. Again, this phenomenon may be the cause of over-estimations of

913 the flooding extent. These two important aspects should be considered in further improvements

914 of the method.

915

916 For the case studies presented in this paper, it took five hours to produce the RP map, which

917 covers an area of ~ 90 ha (~ 0.32 square miles), with a spatial resolution of one metre. The

918 production time of the RP map depends on the size of the study area considered and the spatial

919 resolution required by the users: the larger the study area and the finer the spatial resolution,

920 the longer the production time will be. However, such maps can be produced in advance for

921 areas known to be flood-prone, or while waiting for reception of the SAR flood image. They can

922 also be re-used for other flood scenarios in the same area as long as land use and land cover

923 remain unchanged. Finally, the overall time required for the near-real-time processing operation

924 is very short: for the study area considered in the May 7 case study, the running time of the

925 near-real-time process was less than 25 min on an Intel ® Core ™ i5 CPU (2.40 GHz and

926 6.00 GB RAM).

927 These characteristics confirm that the proposed method for flood extent mapping in urban and

928 rural areas is suited for near-real-time operations and has the potential to be a valuable tool for

929 emergency management during flooding. However, the method has not yet been automated

930 and still requires user interactions for the segmentation of the SAR image. Even if the

931 parameters of the scale, shape and compactness criteria of the multi-resolution segmentation

932 module of the eCognition Developer 8 software might not change much from one SAR flood

933 image to another, they will have to be set manually. If the user is satisfied with the segmentation

934 results obtained with the parameter values identified in this paper, the latency should be short (a

935 few minutes). However, manually setting different parameter values can greatly increase

936 latency. Therefore, in order to make method entirely compatible with emergency management

937 requirements and to reduce the latency resulting from this manual step, the development of an

938 alternative option for automatic segmentation of the SAR images must be considered. Further

939 research will focus on this point.

940 Improvements of the method for RP data at each point of the study area, which proved to be the

941 source of many misclassifications in urban and rural areas, will also be considered. In particular,

942 a method to check the consistency of water elevations at the points along shorelines will be

943 integrated in the method, in order to avoid inconsistencies as the one identified in Fig. 11A.

944 Moreover, the proposed method assumes linear transition between RP water elevations points.

945 This type of transition was selected because it is a very common method of estimating the

946 relationship between RP and water levels, and because it often provides a good estimation of

947 this relationship (Vogel et al., 2011). It also has the advantage of being simple to implement.

948 However, we are aware that it may not be applicable for all river floodplains. Therefore, it would

949 be worth integrating an option for non-linear transition between RP water elevations points in

950 the method for flood return period map generation.

951 It is also worth mentioning that the method was tested on a flooding event with constant linear

952 floodplain geometry and in an urban area with a simple pattern (building of limited heights,

953 streets organized in a grid pattern and no large parking lots close to the river channel).

954 Therefore, in order to verify its robustness, the method needs to be tested in urban areas with

955 contrasting patterns, with different floodplain geometries and more complex flooding dynamics.

956 Finally, to further improve the method and to make it applicable to a large number of flooding

957 events with varying characteristics, a technique to deal with non-bimodal histograms of image

958 objects mean backscatter values should be developed.

959

960

961

6. Conclusion

In this study, an innovative approach for near-real time flood mapping in urban and rural areas, combining the capacity of SAR satellite imagery (C-band, HH polarization) for open water detection and RP data, was presented. The aim was to demonstrate that hydraulic data, which has never been combined with SAR imagery in a method for flood mapping, enables the detection of flooded pixels to be deducted in areas where SAR remote sensing has limitations. The proposed method was applied to two very high resolution RADARSART-2 images (C-band, HH polarization) with different acquisition parameters and water-surface conditions acquired during the 2011 Richelieu River flood (Canada). Classification accuracies achieved in urban and rural areas proved that this method precisely detects flooded areas, even when SAR-derived open water classification —from which RP is extracted— is affected by waves and ripples. The method also addresses the problem of over-detections due to the shadow effect and permanent water surface-like radar response areas, by efficiently removing areas with such characteristics from open water classification using their RP information and their degree of membership to the "open water" set. These results demonstrate that the presented method competes with existing algorithms in terms of urban and rural flood mapping precision. They also highlight the relevance of integrating explicit hydraulic data in a SAR-based flood extent mapping approach. However, further improvements and tests with different flooding scenarios are still necessary to make the method entirely automatic and compatible with emergency management requirements.

References

Altman, N. S. (1992). An introduction to kernel and nearest-neighbor nonparametric regression. *The American Statistician, 46,* 175-185. http://dx.doi.org/10.1080/00031305.1992.10475879

Bhatt, C. M., Rao, G. S., Farooq, M., Manjusree, P., Shukla, A., Sharma, S. V. S. P., Kulkarni, S. S., Begum, A., Bhanumurthy, V., Diwakar, P. G., Dadhwal, V. K. (2016). Satellite based assessment of the catastrophic helum floods of September 2014, Jammu & Kashmir, India. *Geomatics, Natural Hazards and Risk.* 1-19. http://dx.doi.org/10.1080/19475705.2016.1218943

Blaschke, T., Hay, G. J., Kelly, M., Lang, S., Hofmann, P., & Addink, E. (2014). Geographic object-based image analysis – Towards a new paradigm. *ISPRS   Journal of Photogrammetry and Remote Sensing, 87,*180-191. http://dx.doi.org/10.1016/j.isprsjprs.2013.09.014

1007 Blaschke, T. (2010). Object based image analysis for remote sensing. *ISPRS Journal of*

1008 *Photogrammetry and Remote Sensing, 65*, pp. 2-16.

1009 http://dx.doi.org/10.1016/j.isprsjprs.2009.06.004

1010 Boni, G., Candela, L., Castelli, F., Dellepiane, S., Palandri, M., Persi, D., Pierdicca, N., Rudari,

1011 R., Serpicio, S., Siccardi, F., & Versache, C. (2009). *The OPERA Project: EO-based flood risk*

1012 *management in Italy*. Proceedings of the IEEE International Geoscience and Remote Sensing

1013 Symposium (IGARSS) 2009, 12-17 July 2009, Cape Town, South Africa (pp. II-929- II-932).

1014 http://dx.doi.org/10.1109/IGARSS.2009.5418250

1015 Brisco, B., Touzi, R., Van der Sanden, J. J., Charbonneau, F., Pultz, T. J., & D'Iorio, M. (2008).

1016 Water resource applications with RADARSAT-2 – A preview. *International Journal of Digital*

1017 *Earth, 1,* 130-147. http://dx.doi.org/10.1080/17538940701782577

1018 CEHQ – Centre d'Expertise Hydrique du Québec (2006). Révisions des cotes de crues, Rivière

1019 Richelieu, du Sud et baie Missisquoi. *Ministère du Développement durable, de l'Environnement*

1020 *et des Parc*. Québec, Canada.

1021 Chini, M., Pulvirenti, L., & Pierdicca, N. (2012). Analysis and interpretation of the COSMO-

1022 SkyMed Observations of the 2011 Japan Tsunami. *IEEE Transactions on Geoscience and*

1023 *Remote Sensing, 9*, 467-471. http://dx.doi.org/10.1109/LGRS.2011.2182495

1024 Definiens AG (2011) eCognition Definiens Developer 8.7 User Guide. Trimble (Pub.). Munich,

1025 Germany

1026 Esch, T., Roth A., & Dech, S. (2006). Analysis of urban land use pattern based on high

1027 resolution radar Imagery. *Proceedings of the IEEE International Geoscience and Remote*

1028 *Sensing Symposium (IGARSS) 2006*, 31 July - 4 August 2006, Denver, USA (pp. 3615-3618).

1029 http://dx.doi.org/10.1109/IGARSS.2006.926

1030 Fox, J., & Weisberg,S. (2011). An R companion to applied regression, Second Edition.

1031 Thousand Oaks, CA: Sage.

1032 Giustarini, L., Hostache, R., Matgen, P., Schumann, G. J. P, Bates, P. D., & Mason, D. C.

1033 (2013). A change detection approach to flood mapping in urban areas using TerraSAR-X. *IEEE*

1034 *Transactions on Geoscience and Remote Sensing, 51*, 2417-2430.

1035 http://dx.doi.org/10.1109/TGRS.2012.2210901

1036 Greifeneder F, Wagner W, Sabel D & Naeimi V (2014) Suitability of SAR imagery for automatic

1037 flood mapping in the Lower Mekong Basin. International Journal of Remote Sensing 35(8):2857-

1038 2874. http://dx.doi.org/10.1080/01431161.2014.890299

1039 Henry, J. B., Chastanet, P., Fellah, K., & Desnos Y. L. (2006). Envisat multi-polarized ASAR

1040 data for flood mapping. *International Journal of Remote Sensing, 27*, 1921-1929.

1041 http://dx.doi.org/10.1080/01431160500486724

1042 Horritt, M. S., Mason, D. C., Cobby, D. M, Davenport, I. J., & Bates, P. D. (2003). Waterline

1043 mapping in flooded vegetation from airborne SAR imagery. *Remote Sensing of Environment*,

1044 *85,* 271-281. http://dx.doi.org/10.1016/S0034-4257(03)00006-3

1045 Jarihani, A. A, Callow, J.N, McVicar, T.R, Van Niel, T.G & Larsen, J.R (2015) Satellite-derived

1046 Digital Elevation Model (DEM) selection, preparation and correction for hydrodynamic modelling

1047 in large, low-gradient and data-sparse catchments. *Journal of Hydrology* 524:489-506

1048 http://dx.doi.org/10.1016/j.jhydrol.2015.02.049

1049 Kussul N, Shelestov A, Skakun S, Li G, Kussul O & Xie J (2014) Service-oriented infrastructure

1050 for flood mapping using optical and SAR satellite data. International Journal of Digital Earth

1051 7(10):829-845. http://dx.doi.org/10.1080/17538947.2013.781242

1052   Lopes, A., Nezry, E., Touzi, R., & Laur, H. (1993). Structure detection and statistical adaptive

1053   speckle filtering in SAR images. *International Journal of Remote Sensing, 14*, 1735-1758.

1054   http://dx.doi.org/10.1080/01431169308953999

1055   Macina, F., Bignami, C., Chini, M., & Pierdicca, N. (2006). Exploiting physical and topographic

1056   information within a fuzzy scheme to map flooded area by SAR. *Proceedings of the IEEE*

1057   *International Geoscience and Remote Sensing Symposium (IGARSS) 2006*, 31 July - 4 August

1058   2006, Denver, USA (pp. 1052-1055). http://dx.doi.org/10.1109/IGARSS.2006.271

1059   Martinis S, Kersten J & Twele A (2015) A fully automated TerraSAR-X based flood service.

1060   *ISPRS Journal of Photogrammetry and Remote Sensing 104*,203-212.

1061   http://dx.doi.org/10.1016/j.isprsjprs.2014.07.014

1062   Martinis, S., Twele, A., & Voigt, S. (2011). Unsupervised extraction of flood-induced backscatter

1063   changes in SAR data using markov image modeling on irregular graphs. *IEEE Transactions on*

1064   *Geoscience and Remote Sensing, 49,* 251-263. http://dx.doi.org/10.1109/TGRS.2010.2052816

1065   Martinis, S., Twele, A., & Voigt, S. (2009). Towards operational near real-time flood detection

1066   using a split-based automatic thresholding procedure on high resolution TerraSAR-X dara.

1067   *Natural Hazards and Earth System Sciences, 9,* 303-314. http://dx.doi.org/10.5194/nhess-9-

1068   303-2009, 2009

1069   Mason, D. C., Giustarini, L., Garcia-Pintado, J., & Cloke, H. L. (2014). Detection of flooded

1070   urban areas in high resolution Synthetic Aperture Radar images using double scattering.

1071   *International Journal of Applied Earth Observation and Geoinformation, 28*, 150-159.

1072   http://dx.doi.org/10.1016/j.jag.2013.12.002

1073   Mason, D. C., Schumann, G. J. P., Neal, J. C., Garcia-Pintado, J., & P. D. Bates (2012).

1074   Automatic near real-time selection of flood water levels from high resolution Synthetic Aperture

1075   Radar images for assimilation into hydraulic models: A case study. *Remote Sensing of*

1076   *Environment, 124,* 705-716. http://dx.doi.org/10.1016/j.rse.2012.06.017

1077   Mason, D. C., Speck, R., Devereux, B., Schumann, G. J. P., Neal, J. C., & Bates, P. D. (2010)

1078   Flood detection in urban areas using TerraSAR-X. *IEEE Transactions on Geoscience and*

1079   *Remote Sensing*, 48, 882-894.   http://dx.doi.org/10.1109/TGRS.2009.2029236

1080   Matgen, P., Hostache, R., Schumann, G., Pfister, L., Hoffmann, L., & Savenije, H. H. G. (2011).

1081   Towards an automated SAR-based flood monitoring system: Lessons learned from two case

1082   studies. *Physics and Chemistry of the Earth*, 36, 241-252.

1083   http://dx.doi.org/10.1016/j.pce.2010.12.009

1084   NRC – Natural Resources Canada (2015). Free data – Geogratis. Canada's Land cover.

1085   [Online] Available : http://geogratis.gc.ca/api/en/nrcan-rncan/ess-sst/c7f8b56b-b002-56d8-9955-

1086   9b91c13c27e8.html

1087   OSCQ - Organisation de la Sécurité Civile du Québec (2013). Rapport d'èvènement –

1088   Inondations printanières Montérégie 2011. *Gouvernement du Québec*, september 2013.

1089   [Online]

1090   Available :http://www.securitepublique.gouv.qc.ca/fileadmin/Documents/securite_civile/inondatio

1091   ns_monteregie_2011/rapport_evenement_inondations_monteregie.pdf

1092   Pierdicca, N., Chini, M., Pulvirenti, L., & Macina, F. (2008). Integrating physical and topographic

1093   information into a fuzzy scheme to map flooded area by SAR. *Sensors, 8*, 4151-4164.

1094   http://dx.doi.org/10.3390%2Fs8074151

1095   Public Safety Canada (2014). National Floodplain Mapping Assessment, Final Report.

1096   Government of Canada, 68p.

1097   Pulvirenti, L., Chini, M., Pierdicca, N., & Boni, G. (2015). Use of SAR data for detecting flood

1098   water in urban and agricultural areas: the role of the interferometric coherence. *IEEE*

1099   *Transactions on Geoscience and Remote Sensing, 54*, 1532-1534.

1100   http://dx.doi.org/10.1109/TGRS.2015.2482001

1101   Pulvirenti, L., Marzano, F. S., Pierdicca, N., Mori, S., & Chini, M. (2014). Discrimination of water

1102   surfaces, heavy rainfall, and wet snow using COSMO-SkyMed observations of severe weather

1103   events. *IEEE Transactions on Geoscience and Remote Sensing, 52*, 858-869.

1104   http://dx.doi.org/10.1109/TGRS.2013.2244606

1105   Pulvirenti, L., Pierdicca, N., Chini, M., & Guerriero L. (2011). An algorithm for operational flood

1106   mapping from Synthetic Aperture Radar (SAR) data using fuzzy logic. *Natural Hazards and*

1107   *Earth System Science, 11*, 529-540. http://dx.doi.org/10.5194/nhess-11-529-2011

1108   Pulvirenti, L., Pierdicca, N., Chini, M., & Guerriero, L. (2013). Monitoring flood evolution in

1109   vegetated areas using COSMO-SkyMed data: the Tuscany 2009 case study. *IEEE Journal of*

1110   *Selected Topics in Applied Earth Observations and Remote Sensing, 6,* 1807-1816.

1111   http://dx.doi.org/10.1109/JSTARS.2012.2219509

1112   Schumann, G., Bates, P. D., Di Baldassarre, G., & Mason, D. C. (2012). The use of radar

1113   imagery in riverine flood inundation studies. In P. E. Carbonneau & H. Piégay (Ed.), *Fluvial*

1114   *Remote Sensing for Science and Management* (pp. 115-140). Chichester, UK: John Wiley &

1115   Sons, Ltd. http://dx.doi.org/10.1002/9781119940791.ch6

1116   Schumann, G., Bates, P. D, Horritt, M. S., Matgen, P., & Pappenberger, F. (2009). Progress in

1117   integration of remote sensing-derived flood extent and stage data and hydraulic models.

1118   *Reviews of Geophysics, 47*, 1-20. http://dx.doi.org/10.1029/2008RG000274

1119   Schumann, G., Neal, J. C., Mason, D. C., & Bates, P. D. (2011). The accuracy of sequential

1120   aerial photography and SAR data for observing urban flood dynamics, a case study of the UK

1121   summer 2007 floods. *Remote Sensing of Environment, 115*, 2536-2546.

1122   http://dx.doi.org/10.1016/j.rse.2011.04.039

1123   Senthilnath, HJ., Shenoy, H.V., Rajendra, R., Omkar, S.N., Mani, V., Diwakar, P.G. (2013).

1124   Integration of speckle de-noising and image segmentation using Synthetic Aperture Radar

1125   image for flood extent extraction. *Journal of Earth System Science, 122(3)*, 559-572.

1126   Sibson, R. (1981). A brief description of natural neighbor interpolation. In V. Barnett (Ed.).

1127   *Interpolating Multivariate Data, 2* (pp. 21-36). New York: Wiley and Sons.

1128   Soergel, U. (2010). Review of radar remote sensing on urban areas. In U. Soergel (Ed.),

1129   *Remote Sensing and Digital Image Processing 15* (pp. 1-47). Netherlands: Springer Sciences.

1130   http://dx.doi.org/10.1007/978-90-481-3751-0

1131   Speck, R., Turchi, P., & Süß, H. (2007). An end-to-end simulator for high-resolution spaceborne

1132   SAR systems. *Proceedings of SPIE Defense Security, 6568*, 65680H-65680H.

1133   http://dx.doi.org/10.1117/12.717222

1134   Ulaby, F. T., Moore, R., & Fung, A. (1986). Microwave remote sensing, active and passive:

1135   volume scattering and emission theory, advances system and applications. Adisson-Wesley

1136   (Ed.). Norwood, MA: Artech House.

1137   Vogel, R.M., Yaindl, C., Walter, M. (2011). Nonstationarity: flood magnification and recurrence

1138   reduction factors in the United States. *Journal of the American Water Resources Association,*

1139   *47(3)*, 464-474.

1140   http://dx.doi.org/10.1111/j.1752-1688.2011.00541.x

1141   Voigt, S., Martinis, S., Zwenzner, H., Hahmann, T., Twele, A., & Schneiderhan, T. (2008).

1142   Extraction of flood masks using satellite based very high resolution SAR data for flood

1143   management and modeling. *Proceedings of the 4th International Symposium on Flood Defence*,

1144   2008, 6-8 May 2008,Toronto, Canada (pp 27/1 -27/8).

1145   Zhang, J., Zhou, C., Xu, K., Watanabe, M. (2002). Flood disaster monitoring and evaluation in

1146   China. *Global Environmental Change Part B: Environmental Hazards, 2-3*, 33-43.

1147   http://dx.doi.org/10.1016/S1464-2867(03)00002-0